

Machine Learning for Methane Detection and Quantification from Space - A survey

Enno Tiemann^{a,b,f}, Shanyu Zhou^c, Alexander Kläser^b, Konrad Heidler^a, Rochelle Schneider^d, Xiao Xiang Zhu^{a,e}

^a*Data Science in Earth Observation, Technical University of Munich, Arcisstraße 21, Munich, 80333, Germany*

^b*OHB Digital Connect GmbH, Bremen, Germany*

^c*University of Valencia, Valencia, Spain*

^d*Φ-lab, European Space Agency, Frascati, Italy*

^e*Munich Center for Machine Learning, Munich, Germany*

^f*Address correspondence to: enno.tiemann@tum.de,*

Abstract

Methane (CH₄) is a potent anthropogenic greenhouse gas, contributing 86 times more to global warming than Carbon Dioxide (CO₂) over 20 years, and it also acts as an air pollutant. Given its high radiative forcing potential and relatively short atmospheric lifetime (9±1 years), methane has important implications for climate change, therefore, cutting methane emissions is crucial for effective climate change mitigation.

This work expands existing information on operational methane point source detection sensors in the Short-Wave Infrared (SWIR) bands. It reviews the state-of-the-art for traditional as well as Machine Learning (ML) approaches. The architecture and data used in such ML models will be discussed separately for methane plume segmentation and emission rate estimation. Traditionally, experts rely on labor-intensive manually adjusted methods for methane detection. However, ML approaches offer greater scalability. Our analysis reveals that ML models outperform traditional methods, particularly those based on convolutional neural networks (CNN), which are based on the U-net and transformer architectures. These ML models extract valuable information from methane-sensitive spectral data, enabling a more accurate detection. Challenges arise when comparing these methods due to variations in data, sensor specifications, and evaluation metrics. To address this, we discuss existing datasets and metrics, providing an overview of available resources and identifying open research problems. Finally, we explore potential future advances in ML, emphasizing approaches for model comparability, large dataset creation, and the European Union's forthcoming methane strategy.

1. Introduction

Methane (CH_4) is the second most significant anthropogenic greenhouse gas and a precursor to tropospheric ozone, which functions as both another greenhouse gas and an air pollutant (European Parliament WG, 2021; Rouet-Leduc and Hulbert, 2024). Methane is also a potential air pollutant, contributing to premature deaths and reductions in agricultural yields (Staniaszek et al., 2022; European Parliament WG, 2021). Due to its high radiative forcing potential and relatively short atmospheric lifetime of approximately 9 ± 1 years, mitigating methane emissions is prioritized as an effective strategy for combating climate change over decades (Etminan et al., 2016; Irakulis-Loitxate et al., 2021; Prather et al., 2012; IMEO, 2022; Shindell et al., 2012). Methane has accounted for about 30% of observed global warming (IEA, 2022), with a global warming potential 86 times that of CO_2 over 20 years (European Parliament WG, 2021). Atmospheric methane levels have nearly tripled since preindustrial times (Irakulis-Loitxate et al., 2021). The most significant sources of anthropogenic methane emissions are agriculture (approximately 142 Mt), the energy sector (oil, gas, coal, and bioenergy) with 128 Mt, and the waste sector with 71 Mt as of 2023 (IEA, 2024). Emissions exceeding 25 kg/h, known as super-emitters, provide a substantial impact on the overall methane budget (Vaughan et al., 2024; Zavala-Araiza et al., 2015). In the US natural gas supply chain, super-emitters account for over 60% of the energy sector’s total emissions (Duren et al., 2019). Thus, reducing super-emitters is crucial for rapid, cost-effective climate change mitigation (Lauvaux et al., 2022). Consequently, over 110 countries have signed the Global Methane Pledge, committing to a 30% reduction in methane emissions by 2030 (Jacob et al., 2022). The European Union has supported this initiative by funding the International Methane Emissions Observatory (IMEO) and the Methane Alert and Response System (MARS), underscoring the current emphasis on methane monitoring. Methane emissions in the oil and gas sector result from extraction, processing, and delivery through both intentional (e.g., venting and flaring) and unintentional (e.g., equipment leaks) activities (IMEO, 2022). Emissions are typically calculated using bottom-up approaches, starting from the average emissions of facilities multiplied by the number of such facilities (Jacob et al., 2022). Various inventories, such as the Global Fuel Emissions Inventory (GFEI) (Scarpelli et al., 2022) and Emission Database for Global Atmospheric Research (EDGAR) V6 (Monforti Ferrario et al., 2021), are available for different sectors. Still, these inventories often underestimate emissions compared to top-down global observations, leading to significant uncertainties in policy decision-making (Thorpe et al., 2020; Chen et al., 2022; Yu et al., 2022; Rouet-Leduc and Hulbert, 2024).

Satellites are frequently used as fast, cost-effective detection systems for top-down methane inventories due to their high spatial coverage and ability to observe large areas and individual super-emitter plumes. Two types of satellite instruments are employed for methane detection and quantification: infrared sounders in the Thermal Infrared (TIR) range (8000-15000 nm) for vertical methane profiles and spectrometers in the Short-Wave Infrared (SWIR) range (1400-3000 nm) for surface emissions

(Worden et al., 2013; Gorroño et al., 2023; Pandey et al., 2023; Zhang et al., 2022; Irakulis-Loitxate et al., 2022). TIR instruments are generally used for methane estimation in the upper and middle atmosphere, while SWIR instruments are more suitable for detecting surface emissions (Li et al., 2024). This study focuses on surface emissions, specifically, those spectroscopy systems operating in the SWIR range. Within the SWIR range, there are two significant absorption bands at approximately 1650 nm and 2300 nm, necessitating different approaches for detection due to varying gas absorptions (Li et al., 2024).

Methane detection can be divided into three tasks: (1) detecting and calculating methane column concentration per pixel, (2) segmenting methane plumes, and (3) estimating the emission rate and location of the emitting source (Jacob et al., 2016, 2022). Traditional methods and Machine Learning (ML) approaches differ significantly in tackling these tasks.

Traditional methods for detecting and calculating methane column concentration per pixel involve the physical inversion of measured radiance using techniques such as band ratios (Růžička et al., 2023), multi-band multi-pass methods (Varon et al., 2021), and linear multiple regression for multispectral instruments (Sánchez-García et al., 2022; Růžička et al., 2023). Hyperspectral instruments often employ matched filter methods (Foote et al., 2020; Irakulis-Loitxate et al., 2021; Guanter et al., 2021; Thorpe et al., 2016). These approaches are typically computationally expensive and require manual inspection. In contrast, ML methods provide scalability for the detection process, utilizing data from multispectral radiance (Rouet-Leduc and Hulbert, 2024), methane column concentrations (Radman et al., 2023; Vaughan et al., 2024; Růžička et al., 2023), band ratios (Rouet-Leduc et al., 2023), processed hyperspectral data (Růžička et al., 2023; Jongaramrungruang et al., 2022), and hyperspectral radiance data (Kumar et al., 2023, 2020; Joyce et al., 2023).

Traditional methods for segmenting methane plumes rely on predefined rules and thresholds. These methods use concentration thresholds, wind direction, minimum plume size, and other manually designed features to identify and segment plumes (Guanter et al., 2021; Jacob et al., 2022; Gorroño et al., 2023). ML approaches, on the other hand, use advanced algorithms to automatically segment methane plumes if learned from training data. These methods can handle multispectral radiance data, methane column concentrations, and other relevant data types without the need for manual threshold setting, making the segmentation process more efficient and accurate (Schuit et al., 2023; Vanselow et al., 2024; Jongaramrungruang et al., 2022; Rouet-Leduc and Hulbert, 2024).

Estimating emission rates traditionally employs the Integrated Mass Enhancement (IME) method, which calculates emission rates based on methane column concentration, plume size, and wind information (Frankenberg et al., 2016; Varon et al., 2018). This method can be accurate but is often labor-intensive and requires the availability of high-quality input data. ML methods streamline this process by estimating emission rates directly from enhancement maps or using inputs similar to those in

the IME model. These approaches can quickly analyze large datasets and provide accurate emission rate estimates without extensive manual involvement and checks (Jongaramrungruang et al., 2022; Radman et al., 2023; Bruno et al., 2023).

The current state-of-the-art in the literature suggests that ML approaches offer scalable, automated, efficient, and potentially more accurate alternatives, utilizing various types of radiance and concentration data to achieve their tasks while traditional methods for methane detection, segmentation, and emission rate estimation rely heavily on manual processes and predefined rules.

While ML models rely on different architectures, a common challenge persists in the availability of large amounts of high-quality training data. Researchers have adopted different strategies to provide training data in the context of plume mask generation. Some authors rely on manually annotated masks (Schuit et al., 2023; Vaughan et al., 2024; Kumar et al., 2023; Růžička et al., 2023), while others utilize simulated data for training (Bruno et al., 2023; Jongaramrungruang et al., 2022; Radman et al., 2023; Joyce et al., 2023; Rouet-Leduc and Hulbert, 2024). However, when it comes to estimating emission rates, the situation becomes more challenging. Ground truth data for emission rates is scarce, as it is primarily derived from controlled release experiments (Sherwin et al., 2024). Unfortunately, this limited ground truth data is inadequate for ML training purposes. Consequently, researchers have turned to simulated datasets, which suffer from sparsity regarding sample diversity. They lack variation in backgrounds, geographical locations, plume characteristics, wind speeds, emission rates, and real-world data. Addressing these limitations is crucial for advancing ML-based plume analysis and emission estimation.

Most ML models for methane tasks are task-specific (e.g. only for plume segmentation), allowing the use of traditional methods for other tasks (e.g. emission rate estimation), often involving manual expert verification of the ML output. These models, primarily based on Convolutional Neural Networks (CNN), have demonstrated enhanced detection capabilities and accuracy compared to traditional methods (Schuit et al., 2023; Bruno et al., 2023; Jongaramrungruang et al., 2022; Rouet-Leduc and Hulbert, 2024; Vaughan et al., 2024; Růžička et al., 2023; Joyce et al., 2023). However, as mentioned above, they require large amounts of training data and are specialized to specific sensors.

This work focuses on ML approaches for methane detection and extends previous studies (Jacob et al., 2016, 2022) by reviewing state-of-the-art methods and recent developments. In addition to the previous studies, we expand the current and future sensors for methane monitoring and provide a comparison for methane detection. Next, this review provides a first comprehensive review of ML methods, and it reviews used metrics for comparability of different approaches and available datasets in this context. In the end, this work compares traditional methods and discusses future trends and approaches for improving ML models.

2. Sensors for Methane Monitoring

This section summarizes and discusses the operational satellites and instruments utilized for methane monitoring. The systems can be broadly classified into *area flux mappers* and *point-source mappers*. *Area flux mappers* observe large areas to detect changes at country or regional levels, focusing on measuring more significant methane emissions. Satellites such as Sentinel-5 Precursor (Sentinel 5P), Greenhouse Gases Observing Satellite (GOSAT), and Sentinel 3 fall into this category. On the other hand, *point-source mappers* are designed to observe single plumes and estimate their size and emission rate. These instruments offer smaller observation areas but higher spatial resolution, enabling the detection of smaller plumes. Satellites like Sentinel 2, Landsat 8/9, Worldview-3, GHG-Sat constellation, Pecursore Iperspettrale della Missione Applicativa (PRISMA), Environmental Mapping and Analysis Program (EnMAP), and Airborne Visible Infrared Imaging Spectrometer - Next Generation (AVIRIS-NG) are examples of *point-source mappers*. Furthermore, methane monitoring systems can be categorized based on the number of spectral bands they employ. Multispectral systems utilize a few larger bands, while hyperspectral systems utilize many bands with small bandwidths. Examples of multispectral systems include Sentinel 5P, Geostationary Operational Environmental Satellites (GOES), GOSAT, Sentinel 3, Sentinel 2, Landsat 8 and 9, Worldview-3, and GHGSat. Hyperspectral systems encompass PRISMA, EnMAP, AVIRIS-NG, Earth Surface Mineral Dust Source Investigation (EMIT), and others in development. For multispectral satellites, spatial resolution is crucial for detecting plume sizes, while area flux mappers prioritize spectral resolution for accurate measurements at the cost of spatial resolution. The different missions are illustrated in Figure 1 and plotted by Ground Sampling Distance (GSD) with categorization into hyper-/multispectral.

Figure 1 shows that satellites designed for larger areas are predominantly multispectral, offering limited bands tailored to each specific product and use case. Another finding is that hyperspectral satellites primarily feature a 30 m spatial resolution (with exceptions such as EMIT mounted on the International Space Station (ISS), Aurora as a commercial satellite and AVIRIS-NG as an airborne sensor). This illustrates the trade-off between spatial and spectral resolution, aiming to strike a balance that ensures adequate resolution for widely used applications in remote sensing. The Chinese GaoFen 5 satellite is listed two times in Figure 1 as the satellite carries two instruments for methane observation (the multispectral Greenhouse-gases Monitoring Instrument (GMI) and the hyperspectral Advanced Hyperspectral Imager (AHSI) instruments).

Detailed information on the different systems for methane observations is listed in Table 1. All mentioned systems measure the radiance of solar backscatter in the SWIR band for methane detection, with standard spectral bands ranging from 1630 to 1700 nm (1650 nm band) or 2200 to 2400 nm (2300 nm band) (Jacob et al., 2022). All satellites operate on a sun-synchronous, low-earth orbit except for GOES, which is on a geostationary orbit, providing images only during daylight hours. Operational

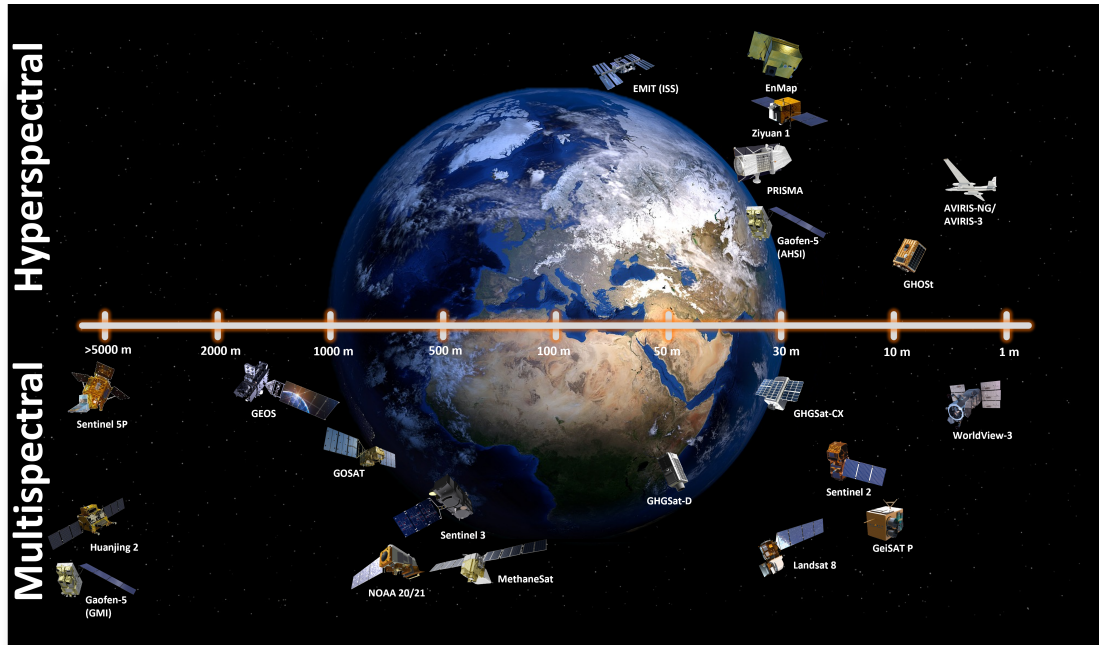


Figure 1: Overview of existing methane monitoring systems with categorization according to GSD and categorization into multi- and hyperspectral missions.

modes typically involve either pointing capabilities, offering a narrow swath with higher spatial resolution, or push-broom imaging, covering the entire globe continuously at the expense of spatial resolution. Worldwide coverage is provided by Sentinel 5P, GOES, GOSAT, Sentinel 3, Sentinel 2 and Landsat 8/9. The not-mentioned satellites provide pointing capabilities that need specific tasking and, as a result, do not consistently monitor the exact location on Earth continuously.

The *organizations* of the second column in Table 1 are China National Space Agency (CNSA), China Center for Resources Satellite Data and Application (CRESDA), China Academy of Space Technology (CAST), European Space Agency (ESA), National Oceanic and Atmospheric Administration (NOAA), National Aeronautics and Space Administration (NASA), Jet Propulsion Laboratory (JPL), Japan Aerospace Exploration Agency (JAXA), New Zealand Space Agency (NZSA), European Defence Fund (EDF), Italian Space Agency (ASI), German Aerospace Center (DLR), United States Geological Survey (USGS). The *End of Life (EOL)* column indicates the planned termination of the mission, typically representing the minimum required lifetime, which is often extended by a few years. The column *GSD* describes the ground dimensions of one pixel looking directly at the Earth (nadir). The *Swath* describes the covered ground distance vertical to the Azimuth (Flight line). The provided *revisit time* describes the time necessary to measure a specific location a second time, which correlates especially with the constellation size of the different missions and the satellites' pointing capabilities. The *methane band* denotes the potential

spectral ranges of sensors that could theoretically be utilized for methane monitoring, even though such utilization might not have been realized so far or is less feasible or impractical compared to other methane bands. From these spectral bands, the *spectral resolution* describes the difference between the upper- and lower bound of the Full Width at Half Maximum (FWHM) (or best approximation) or the spectral sampling in the case of hyperspectral instruments. It is worth mentioning that some satellites like GHGSat provide multiple spectral bands in the 1650 nm area. The *product levels* typically encompass the top of the atmosphere (L1), methane concentration per pixel or enhancement maps (L2), methane plume mask (L3), and emission rate/emission location (L4). The *data policy* is named as governmental (gov), open access (open), commercial (com), or scientific use (sci).

While most satellites are not designed explicitly for methane measurements, multiple satellites offer Level 2 methane data, facilitating access to data for further analysis and ML applications.

Table 1: Satellite Overview sorted by GSD

Mission /Instrument	Organization	launch date (EOL)	GSD (Nadir)	Swath (km)	revisit time	Methane band (nm)	spectral resol. (nm)	data policy	Product	Ref
Gaofen 5 /GMI	CNSA	2021 (2028) 2022 (2030)	10.5 km	750	5 d	1650	16	gov	L1	Ge et al. (2022) Ye et al. (2023)
Huanjiang 2 /POSP	CRESDA, CAST	2020 (2025)	6 km	800	4 d	1650 2300	-	gov	L1	Sherwin et al. (2024) Dubovik et al. (2019)
Sentinel 5P /TROPOMI	ESA	2017 (2027)	5.5 x 7 km	2600	daily	2300	0.25	open	L2	Fletcher (2016)
GOES /ABI	NOAA, NASA	2018 (2028) 2022 (2035)	1-2 km	Western Hemisphere	<1 d	1650 2300	4 5	open	L2	Schmitt et al. (2018) Watine-Guiu et al. (2023)
GOSAT /TANSO-FTS	JAXA	2009 (2023) 2018 (2023)	1500 m 920 m	786 920	3 d 6 d	1650	0.06	open	L2	Schmitt et al. (2017) Imasu et al. (2023)
NOAA-20/21 VIIRS	NOAA, NASA, EUMETSAT	2017 (2027) 2022 (2030)	750 m	3000	<1 d	1650 2300	60 (63) 54 (48)	open	L1	de Jong et al. (2024)
Sentinel 3 /SLSTR	ESA	2016 (2026) 2018 (2028)	500 m	1400	1-2 d	1650 2300	60 50	open	L1	Donlon et al. (2012) Fletcher (2012b)
MethaneSAT	NZSA, EDF	2024 (2028)	100 x 400 m	260	3-4 d	1650	0.25	open	L1, L2, L4	Staebl et al. (2021) Chulakadabba et al. (2023)
EMIT	NASA	2022 (2025)	60 m	80	36.5 d	1650 2300	7-4	open	L1, L2	Thompson et al. (2024) Thorpe et al. (2023)
GHGSat(D) /WAF-P	GHGSat Inc.	2016 (2024)	50 m	15	14 d	1650	~0.1	com	L2, L3	Varon et al. (2019) Jervis et al. (2021)
PRISMA /HYC	ASI	2019 (2024)	31 m	31	7-29 d	1650 2300	6.5-11	open	L1	Coghetti et al. (2021) Guanter et al. (2021)
GHGSat(CX) /WAF-P	GHGSat Inc.	2020 (2024) multiple (2027)	30 m	15	1-2 d	1650	~0.1	com	L2, L3	Varon et al. (2019) Jervis et al. (2021)
Gaofen 5 /AHSI	CNSA	2021 (2028) 2022 (2030)	30 m	60	5 d	1650 2300	10	gov	L1	Liu et al. (2019)
Ziyuan 1-02D/E /AHSI	CRESDA	2021 (-) 2019 (-)	30 m	60	1-3 d	1650 2300	20	gov	L1	Song et al. (2022) Sherwin et al. (2024)
EnMAP /HSI	DLR	2022 (2026)	30 m	30	4 - 27 d	1650 2300	10	Sci	L1	Yang et al. (2022) Chabrilat et al. (2022)
Landsat 8/9 /OLI	NASA, USGS	2013 (2028) 2021 (2031)	30 m	185	~8 d	1650 2300	85 185	open	L1	Li and Roy (2017) Ihlen (2019) Sayler (2022)
Sentinel 2 /MSI	ESA	2015 (2025) 2017 (2027)	20 m	290	<5 d	1650 2300	90 180	open	L1	Gorroño et al. (2023) Fletcher (2012a)

Table 1: Satellite Overview sorted by GSD (continued)

Mission /Instrument	Organization	lauch date (EOL)	GSD (Nadir)	Swath (km)	revisit time	Methane band (nm)	spectral resol. (nm)	data policy	Product	Ref
GeiSAT P /iSIM-90	SATLANTIS Orbital	2023 (2027)	13 m	16.5	-	1650	-	com	-	Ubierna et al. (2022) EO Portal (2024)
Aurora/GHOS/HI	Sidekick Inc. Maxar	2021 (2026) 2023 (2029)	8 m	-	<1 d	1650 2300	~ 4.1	com	-	WMO (2024) CEOS (2024a)
WorldView-3	Technologies Inc.	2014 (2024)	3.7 m	13.1	~1 d	1650 2300	40 50, 70	com	L1	Sánchez-García et al. (2022)
AVIRIS-NG /((Air)	NASA, JPL	2014	~3 m	~1.85	airborne	1650 2300	5	open	L1	Cusworth et al. (2019) Thorpe et al. (2016)
AVIRIS-3 /((Air)	NASA, JPL	2023	~2 m	~2.1	airborne	1650 2300	7.5	open	L1	Thorpe et al. (2014) Green et al. (2022)

Some satellites mentioned in Table 1 provide limitations or changes that can not be assessed from the Table. Sentinel 5P’s resolution changed from 7.5 km x 7.5 km to 5.5 km x 7.5 km on 06. August 2019. The specifications of the satellites NOAA-20 and NOAA-21 differ slightly, so the spectral resolution in Table 1 shows the resolution of NOAA-21 in parentheses. The EMIT instrument is mounted on the ISS, limiting the mapping area from 51.6° to -51.6° latitude and providing a long revisit time of 36.5 days for some points. MethaneSAT has just been launched and is still in the commissioning phase at the time of writing. This is why the processing levels are estimated, and the operational instrument performance has not been proven yet. Landsat 8 and Landsat 9 are different satellites, but the Operational Land Imager (OLI) instruments provide similar optics, which is why the data is similar, and algorithms can be applied for both. The Satellites Gaofen 5, Huanjing 2, and Ziyuan 1 are usually just for the organizations’ use. However, the satellites are included in this list due to a more open data policy for the work of Sherwin et al. (2024). The GHGSat-CX constellation consists of the satellites GHGSat-C1 to GHGSat-C10 for methane monitoring, providing a high revisit time through the number of satellites and pointing capabilities. Due to limited publicly available information, some information is missing for the commercial missions GeiSAT Precursor (GeiSAT P) and Aurora / Global Hyperspectral Observation Satellite (GHOSat). The mission GOES refers to GOES-16 (East) and GOES-18 (West), with GOES-17 as an on-orbit standby satellite, which are the only geostationary satellites for methane monitoring so far. These satellites provide coverage from 150° to 0° longitude. Worldview-3 provides multiple bands sensitive to methane, two of which provide different spectral resolutions in the 2300 nm band; one band provides 50 nm spectral resolution and another one 70 nm. Both AVIRIS sensors provide a GSD of 0.3 to 20 m depending on the flight height, with a sampling of 0.6 milliradian for AVIRIS-3 and 1 milliradian for AVIRIS-NG. The Swath Angle of AVIRIS-3 and AVIRIS-NG is 40° and 34°, respectively (Green et al., 2022). With the typical flight height of 3 to 4 km from more extensive campaigns (Frankenberg et al., 2016; Duren et al., 2019), we assumed a 3300 m flight height resulting in a GSD of about 3.3 m and Swath of 1.8 km for AVIRIS-NG and 2 m GSD and 2.1 km swath for AVIRIS-3.

As for the products provided by these systems, the main focus is not on targeting methane observations due to the vast availability of Level 1 data. Only Sentinel 5P, GOES, and GOSAT, as well as the Methane-focused missions of MethaneSAT and GHGSat, provide concentration maps that can be used for methane observations. MethaneSAT and GHGSat even provide higher-level methane products using some approaches mentioned hereafter. Even though most satellites provide a methane band of 1650 nm, the predominantly used methane band is 2300 nm as it yields improved results, explained in Chapter 3.1.1. Commercial systems that need to be purchased generally provide a higher revisit time and spatial resolutions due to pointing capabilities than publicly available systems. This reflects the detection limits as described in Chapter 2.2. The downside of free available systems is either the revisit time

(through fewer satellites), GSD, or spectral resolution. GHGSat is the only system that provides a very small bandwidth for the methane-sensitive bands at 1650 nm, with about 0.1 nm providing excellent spatial resolution.

2.1. Future Satellites for methane detection

The increasing attention in recent years for methane monitoring has resulted in multiple satellite missions being able to fulfill this task. In Table 2, we provide an overview of the evolving landscape of satellite-based methane monitoring, focusing on the latest developments in satellite technology and upcoming missions planned for launch. Here, we concentrate on satellite missions, which provide basic information about the instruments used and their performance. In contrast to the mentioned future methane missions in (Jacob et al., 2022), the Geocarb mission has been excluded due to cancellation announced by NASA in 2022 (NASA, 2022). Similarly, the Microcarb mission strongly focuses on CO₂ but removed the methane bands during development (EO Portal, 2016). The systems mentioned in Table 2 and the existing systems all rely on the solar backscatter of the earth to measure methane. However, the Methane Remote Sensing Lidar Mission (MERLIN) instrument is an exception as it emits its own signal and analyses the reflection of the signal to measure methane (Ehret et al., 2017). Table 2 describes the *launch date* as a planned launch or launch dates of multiple satellites for each mission, the *methane band* is the band which will be primarily used for methane detection, *spect resol* is the spectral resolution defined as the FWHM or provided spectral resolution. The columns *revisit time* and *GSD* align with the existing sensors in Table 1. Particular information that is not publicly available has been marked as “-”.

Table 2: Future Satellites for methane monitoring

Mission	Launch date	Methane band (nm)	spect resol in (nm)	revisit time (d)	GSD	Ref
Carbon Mapper	2024	2300	6	1-7	30x30m ² 30x60m ²	Duren et al. (2021)
GOSAT-GW	2024	1650	0.2	3	10km (wide) 1-3km (focus)	NIES (2024)
BrightSkies	2024	1650	<0.5	4	100m	CEOS (2024c)
Tango	2026	1650	0.45	-	300m	Brenny et al. (2023)
TanSat-2	2025	2300	0.11	2-5	2x2km	CEOS (2024b)
GeiSAT (iSIM-170)	2025	2300	-	-	9m	Ubierna et al. (2022)
CO2M	2025/26/27	1650	0.3	5	2x2km ²	Sierk et al. (2021)
Sentinel 5	2025/31/38	both	0.25	daily	7.5x7.5km ²	Irizar et al. (2019)
MERLIN	2027	1650	3x10 ⁻⁴	28	up to 150m ²	Ehret et al. (2017)
CHIME	2028/30	both	<10	10-12.5	20-30m	Candiani et al. (2022)

The GeiSAT instrument, iSIM-170, was already demonstrated in 2020 during a test mounted on the ISS. (Ubierna et al., 2022). The private company GHGSat has planned to launch four more GHGSat-CX satellites, which are not listed here, as they will carry the same instrument as their predecessors. For the same reason, the

planned GOES-19 satellite is not listed here. It carries the same Advanced Baseline Imager (ABI) as the existing GOES satellites. Carbon mapper and Global Observing Satellite for Greenhouse gases and Water cycle (GOSAT-GW) provide two capturing modes, one with a focus and one wider for different use cases, which results in the two different GSDs. The future missions mentioned here show different satellites for large spatial areas and point emissions, building a new and improved baseline for diverse methane detection tasks.

The future missions tend to focus on higher spectral resolution instead of spatial resolution due to the higher spectral resolution compared to existing systems. This may limit the capabilities to detect small plumes but should increase the concentration estimation and potentially the emission rate estimation in the end.

2.2. Comparison of existing sensors for methane detection

The sensors discussed in the preceding parts of Chapters 2 offer diverse functionalities, applications, and capabilities. The primary focus of this section revolves around the detection thresholds of these systems, representing the minimum plume size that can still be detected and quantified in a good-case scenario. This parameter is often called the *minimum point source emission rate* in the literature.

Aligned with a previous study of Jacob et al. (2022), we have adopted certain detection thresholds as well as refined thresholds based on recent research and included systems not mentioned previously. Due to incomplete information regarding the detection thresholds of specific systems, not all future systems could be integrated into the comparative analysis presented in Table 3.

Satellites such as Sentinel 5P or GOSAT are predominantly employed for monitoring country or worldwide emissions at a large scale, benefiting from their high spatial coverage, which results in a high detection threshold. Additionally, systems like GOSAT are utilized to establish monthly or yearly methane emission budgets for large areas. This differs from their application in estimating emission rates of individual plumes. The detection threshold of GOSAT for single-source emission has not been investigated intensively by the scientific community. Therefore, the threshold has been calculated through the theoretical analysis of GOSAT and Sentinel 5P of 7.1 and 4.2 tons per hour (Jacob et al., 2016). Through this relation, we assumed a higher detection threshold for GOSAT as for Sentinel 5P, which was investigated by Lauvaux et al. (2022).

Sentinel 2 and Landsat 8/9's detection thresholds have been adopted to new research by Gorroño et al. (2023) stating a more accurate detection threshold of 1000-5000 kg/h.

Notably, most of these systems were not primarily designed for methane monitoring or point source emissions but provided satisfactory results. Only GHGSat and methaneSAT are precisely engineered with a focus on methane measurement.

Due to the limited access to the Chinese governmental satellite missions Ziyuan 1 and Gaofen 5, public analysis of methane detection thresholds could not be found

during writing. Usually, these satellites are only available to the Chinese government. However, in recent work by Sherwin et al. (2024), three research groups received data on these satellites for comparison. The authors found that both satellites could detect plumes in actual observations with an emission rate of about 1000 kg/h, mentioning that the satellites could detect emissions lower under favorable conditions.

Generally, a lower detection threshold is observed for satellites with lower GSD. Hyperspectral satellites offer superior spectral properties and narrower bands, which proves advantageous in detecting smaller plumes. Dedicated methane detection systems like GHGSat feature very narrow bands in the spectral absorption range of methane (1650 nm), resulting in the lowest detection thresholds achieved by satellites thus far.

Table 3: Methane emission rate thresholds for detection of researched systems

Mission	Detection threshold (kg/h)	GSD (nadir)	type	Ref
GOSAT	>25000	1500 m	multi	Jacob et al. (2016)
Sentinel 5P	25000	5.5x7.5 km	multi	Lauvaux et al. (2022)
Sentinel 3	8000 - 20000	500 m	multi	Pandey et al. (2023)
NOAA-20/21	8000 - 20000	750 m	multi	de Jong et al. (2024)
Sentinel 2	1000 - 5000	20 m	multi	Gorroño et al. (2023), Ehret et al. (2022)
Landsat 8/9	1000 - 5000	30 m	multi	Gorroño et al. (2023), Ehret et al. (2022)
GHGSat-D	1000 - 3000	50 m	multi	Jervis et al. (2021)
PRISMA	500 - 2000	30 m	hyp	Guanter et al. (2021)
Ziyuan 1	<1000	30 m	hyp	Sherwin et al. (2024)
Gaofen 5	<1000	30 m	hyp	Sherwin et al. (2024)
EMIT	200 - 300	60 m	hyp	Thorpe et al. (2023)
EnMAP	100 - 500	30 m	hyp	Cusworth et al. (2019)
GHGSat-CX	100 - 200	30 m	multi	Gauthier (2021)
GeiSAT P (iSIM-90)	~150	13 m	multi	EO Portal (2024)
WorldView 3	<100	3.7 m	multi	Sánchez-García et al. (2022)
AVIRIS-NG (airborne)	2 - 10	~3 m	hyp	Duren et al. (2019), Thorpe et al. (2020)
AVIRIS-3 (airborne)	<10	~2 m	hyp	Coleman et al. (2024)
Tango	10000	100 m	multi	Brenny et al. (2023)
MethaneSAT	500	100x400 m	multi	Jacob et al. (2022)
BrightSkies	100	100 m	multi	CEOS (2024c)
Carbon Mapper	50 - 200	30 m	multi	Duren et al. (2021)
GeiSat (iSIM-170)	~50	9 m	multi	EO Portal (2024)

While the airborne sensor AVIRIS-3 is assumed to provide a better detection threshold to AVIRIS-NG, it is important to note that no work has yet analyzed the actual detection limit of this sensor. However, ongoing research on the detection

capabilities of AVIRIS-3, led by RW Coleman and other researchers (Coleman et al., 2024), holds the potential for future discoveries in methane detection technology.

The future of satellite systems (i.e. the last 5 missions in Table 3) holds great promise. These advancements are about achieving even lower detection thresholds and signify expanding our capabilities to detect increasingly smaller methane plumes. This potential for future advancements should inspire optimism and excitement in environmental science and satellite technology.

3. Traditional approaches for optical satellite-based methane plume detection

Methane can be detected using three primary types of platforms: ground-based, airborne, and satellite-based systems. Among them, satellite-based detection can provide stable and continuous global monitoring of methane emissions (Jacob et al., 2016, 2022). Methane’s selective radiation absorption at approximately 1650 nm and 2300 nm results in distinctive spectral absorption features. Consequently, the retrieval of methane concentrations from satellite observations typically relies on spectrally-resolved measurements of solar radiation reflected by the Earth’s surface within the SWIR region of the spectrum, spanning approximately 1600 to 2500 nm (Worden et al., 2015; Guanter et al., 2021). The previously mentioned satellite systems have been used for methane observations, with multiple more to be launched. This Chapter describes the approaches for detecting and quantifying methane from satellite observations.

3.1. Methane retrieval

The Methane retrieval process aims to determine the enhancement of methane column concentration per pixel with respect to the background (ΔXCH_4), mainly divided into physically-based and statistical methods. Physical-based methodologies explicitly model radiative transfer interactions among the surface, atmosphere, and instrument. Conversely, statistical methods are utilized to extract relevant information from the image.

3.1.1. Physical-based method

Estimating methane concentration enhancement typically involves fitting high-spectral-resolution observations in the SWIR spectral region to a modeled radiance spectrum during a single satellite overpass (Thorpe et al., 2014; Jacob et al., 2016). Physical-based methane concentration enhancement map retrieval involves two primary methods: the *full-physics* retrieval and the *CO₂ proxy retrieval*.

The *full-physics* approach utilizes a radiative transfer model to invert spectra, aiming to simultaneously solve for vertical profiles of methane concentration, aerosol extinction, and surface reflectivity. For this approach the percentage of good estimates of methane concentration per pixel (success rate) using TROPOMI data in the 2300 nm band is only 3% over land (Jacob et al., 2022; Lorente et al., 2021). Besides, this

method faces challenges in capturing vertical gradients and is heavily influenced by atmospheric conditions and surface heterogeneity (Jacob et al., 2022). Conversely, the *CO₂ proxy retrieval* leverages the adjacent CO₂ absorption band at 1610 nm to estimate methane and CO₂ concentrations simultaneously (Frankenberg et al., 2005), achieving similar precision and accuracy (Buchwitz et al., 2015). Despite being faster and less affected by surface and aerosol biases, the method using the GOSAT instrument at 1650 nm still encounters errors in regions with unresolved CO₂ variability and from sources co-emitting methane and CO₂ like flares, achieving a 24% success rate over land applied on GOSAT data, primarily limited by cloud cover (Parker et al., 2020). Research has highlighted that higher spectral resolution enables more precise measurements, as demonstrated by Cusworth et al. (2019) and Jongaramrungruang et al. (2021). Additionally, the positioning of spectral bands relative to methane absorption lines significantly influences precision and accuracy, as quantified by Jacob et al. (2022). Hyperspectral data allows for joint optimization of methane, other trace gases, and surface albedo from a single observation (Jacob et al., 2016; Cusworth et al., 2019; Irakulis-Loitxate et al., 2021; Guanter et al., 2021; Roger et al., 2024), multispectral instruments with broadband channels, despite their lower spectral resolution (typically around 100 nm), can also effectively retrieve methane column concentration enhancements. This is done using two spectral measurements: one that includes methane emissions and one that does not. Dataset recorded by Sentinel 2 has been proved to successfully estimate methane column enhancements in a plume relative to the background by inferring surface reflectivity from adjacent bands around 1600 and 2300 nm, or from observations of the same scene when the plume is absent (Varon et al., 2021; Sánchez-García et al., 2022; Ehret et al., 2022; Gorroño et al., 2023). The main principles could be concluded as below (Varon et al., 2021):

- The Single-Band-Multiple-Pass (SBMP) retrieval method
The SBMP retrieval method compares TOA reflectances from the spectral band (located around 2300 nm) over a methane source to those measured without emissions. It derives methane concentration enhancements from the fractional change in reflectance, adjusted by a scaling factor, and uses a Gauss–Newton method for retrieval (Varon et al., 2021). While conceptually simple, SBMP requires multiple satellite passes and may struggle with identifying plume-free passes for persistent methane sources. It is also sensitive to non-uniform changes in surface albedo over time. However, background water vapor and CO₂ variations have minimal effect on the retrieval process (Duren et al., 2019).
- The Multi-Band-Single-Pass (MBSP) retrieval method
The MBSP retrieval method estimates methane enhancements by comparing reflectances from two adjacent spectral bands (ideally located at 1650 and 2300 nm) during a single satellite pass. It utilizes least-squares fitting to determine the fractional change in reflectance and employs a fractional absorption model

considering methane sensitivity. MBSP offers the advantage of requiring only one satellite pass for methane concentration retrieval but relies on signals from spectral bands with central wavelengths separated by 600 nm, is too wide a gap and could lead to errors due to varying aerosol reflectance properties in the two bands.

- The Multi-Band-Multi-Pass (MBMP) retrieval method
The third retrieval method integrates aspects of the first two, determining methane column enhancements by comparing MBSP retrievals from distinct satellite passes. Here, systematic errors in the MBSP retrieval (MBSP) caused by wavelength separation between bands are rectified by subtracting another MBSP retrieval (MBSP') conducted during a satellite pass devoid of methane plume occurrences. This correction aims to eliminate artifacts inherent in the retrieval field, preserving only genuine methane enhancements if systematic errors in the MBSP retrievals remain consistent across both passes.

The MBMP retrieval method typically achieves superior precision and lower plume detection limits across various scene types. However, in situations with variable surface conditions, where defining a reference is challenging, the single-pass MBSP method shows slightly better performance (Varon et al., 2021).

3.1.2. Statistical methods

Statistical methods offer an alternative approach to methane retrieval by utilizing statistical techniques to constrain the retrieval process with information extracted directly from the image. They comprise methods such as matched-filter and singular vector decomposition concepts and have shown success with imaging spectroscopy data (Thorpe et al., 2014; Thompson et al., 2016; Foote et al., 2020; Guanter et al., 2021; Roger et al., 2024) and multispectral satellite images (Wang et al., 2024). One of the primary advantages of statistical retrievals is their ability to implicitly account for potential radiometric and spectral errors commonly found in satellite imaging spectroscopy data, such as vertical striping from detector non-uniformity (Guanter et al., 2021). In contrast to the physical based model, the statistical models provide (ΔXCH_4) estimates directly without requiring additional background considerations, unlike physically based methods. Additionally, statistical retrievals show substantially superior computational efficiency compared to physically based methods, making them an efficient solution for methane retrieval.

Matched filters are the most used method and have proven to be effective for retrieving methane enhancements from point sources. This technique entails aligning the observed spectrum with a background spectrum that has been convolved with a target methane absorption spectrum, specifically targeting the 2300 nm absorption band. Researchers have extensively applied matched filter methods to identify methane emissions from various sources, including industrial facilities and natural gas infrastructure, utilizing AVIRIS data from studies conducted by Frankenberg et al.

(2016), Duren et al. (2019), and Cusworth et al. (2021). Furthermore, matched-filter methods have been successfully adapted for satellite retrieval of point sources, as shown in studies conducted by Thompson et al. (2016), Guanter et al. (2021), and Irakulis-Loitxate et al. (2021). A vital advantage of these methods is their ability to directly retrieve methane enhancement above the background, offering a quicker alternative to *full-physics* retrieval methods. This efficiency makes matched-filter methods particularly suitable for plume imaging applications, where capturing methane enhancement above the local background is of primary interest.

This technique models the background radiance using a multivariate Gaussian distribution characterized by its mean value (μ) and covariance matrix (Σ). Deviations from the modeled background radiance indicate CH₄ concentration enhancements.

$$x = \mu + \Delta X_{\text{CH}_4} \cdot t \quad (1)$$

The formula relates the at-sensor radiance spectrum (x) to the methane concentration enhancement. The target signature t is obtained by multiplying the mean background radiance (μ) with the unit methane absorption spectrum (k). The k spectrum is computed using the Moderate resolution atmospheric Transmission (MODTRAN) radiative transfer model, which simulates methane transmittance spectra for different mixing ratios. Calculating k requires setting MODTRAN to spectral transmittance mode and applying atmospheric profiles from the U.S. Standard Atmosphere. The fitting process correlates methane enhancements with transmittance changes, and derivatives quantify the absorption corresponding to a unit methane concentration. The calculation integrates over an 8 km vertical column for satellite observations (Thompson et al., 2016). This method is often employed in the 2100–2450 nm spectral range to detect methane. Despite higher radiance levels typically observed in the 1650 nm absorption window, its weaker absorption and fewer spectral bands covering this range lead to noisier methane retrievals (Roger et al., 2024). Although, matched-filters can be used to calculate methane concentration for each pixel within a higher spatial resolution compared to area mappers, on water, low albedo surfaces, and other challenging conditions it still tend to have lower success rate.

3.2. Emission rate estimation

Methane concentrations retrieved via remote sensing are normally described using the column-average dry molar mixing ratio, symbolized as X [ppb]. It characterizes the methane plume by the enhancement ΔX , which is calculated as the deviation of X from the local background concentration X_b . To correlate plume observations with the emission source rate Q [kg h⁻¹], the column mass enhancement $\Delta\Omega$ [kg m⁻²] is a more practical measure. The column mass enhancement $\Delta\Omega$ is related to the enhancement ΔX through the formula:

$$\Delta\Omega = \frac{M_{\text{CH}_4}}{M_a} \Omega_a \Delta X \quad (2)$$

In this equation, M_{CH_4} and M_a represent the molar masses of methane and dry air, respectively, in units of kg mol^{-1} . The variable Ω_a signifies the column amount of dry air, measured in units of kg m^{-2} .

Quantifying point source emissions from satellite observations of instantaneous methane plumes involves a unique inversion challenge. The main objective is to determine the emission rate from a single snapshot of the plume. While the plume’s morphology is influenced by turbulent diffusion and mean wind, the observation typically captures the total methane column, thus minimizing errors related to vertical boundary layer mixing. However, the absence of precise wind speed information poses a significant challenge, as variations in wind speed directly impact concentration ratios in the plume, propagating errors in wind speed estimation to the inferred point source rate. Various methods have been developed to address this challenge (Jacob et al., 2022), including the Gaussian plume model, mass balance method, Gauss theorem method, cross-sectional flux (CSF) method, and IME method. The *CSF* and *IME* methods are most frequently used to derive point source rates from satellite observations, consistently producing reliable results (Krings et al., 2011, 2013; Frankenberg et al., 2016; Varon et al., 2018).

The *CSF* method evaluates emission source rates by calculating the flux in the cross-section of the plume orthogonal to the plume axis, initially applied in aircraft *in situ* observations (Varon et al., 2018) and adapted for remote sensing datasets (Krings et al., 2011; Tratt et al., 2014). While remote sensing offers comprehensive vertical coverage compared to *in situ* methods, it lacks detailed wind characterization, relying on an average vertical wind speed U_{eff} parameterized from the 10-meter wind speed (Varon et al., 2018) or interpolated vertical profiles (Krings et al., 2011). The emission rate Q is given by:

$$Q = U_{eff} \int_{-\infty}^{+\infty} \Delta\Omega(x, y) dy \quad (3)$$

The *IME* method connects the source rate with the total mass of the plume detected downwind, providing a quantitative approach to assess emissions. To calculate the IME of an observed column plume, which consists of N pixels, the sum of the product of the column amount for each pixel and its respective area A_j is computed:

$$\text{IME} = \sum_{j=1}^N \Delta\Omega_j A_j \quad (4)$$

Frankenberg et al. (2016) established an empirical linear relationship between IME and the source rate Q for methane plumes detected in airborne data, utilizing independent estimates from the cross-sectional flux method to define this relationship (Frankenberg et al., 2016). More fundamentally, the connection between IME and Q is determined by the residence time τ of methane in the detectable plume. The residence time τ can be dimensionally represented using an effective wind speed U_{eff}

and a characteristic plume size L :

$$Q = \frac{1}{\tau} \text{IME} = \frac{U_{eff}}{L} \text{IME} \quad (5)$$

Under idealized conditions, U_{eff} and L would directly correspond to the wind speed and plume length, assuming uniform transport to a terminal distance. However, in reality, plume dissipation is driven by turbulent diffusion in all directions. Consequently, U_{eff} and L must be treated as operational parameters that are linked to observational data on wind speed and the spatial extent of the plume. The derivation from synthetic plumes indicates that the detectable plume size L is influenced by both Q and U_{eff} , introducing non-linearity into the equation.

While the CSF method is more physically based and allows for error reduction through cross-sectional analysis, the IME method parameterizes total mass enhancement in the plume relative to wind speed. Both methods require accurate wind speed estimates, typically obtained from meteorological databases or measurements at the point source location, which can dominate the error budget and limit precision to around 30% (Varon et al., 2018).

Another important factor in calculating emission rates is that both methods require the identification and masking (i.e., segmentation) of the plume in the enhancement map. Plume detection and masking in satellite imagery have traditionally relied on pure human analysts (Guanter et al., 2021), but this is impractical for operational use. Semi-automated methods using statistical thresholding and adjacency criteria have been developed to detect methane enhancements above background levels for plume masking (Varon et al., 2019; Duren et al., 2019; Gorroño et al., 2023; Roger et al., 2023b). However, these methods are susceptible to retrieval artifacts, often mistaking surface features for methane plumes (Cusworth et al., 2019; Bruno et al., 2023).

3.3. Drawbacks

Traditional methods for methane plume detection and estimation are significantly hampered by their need for extensive manual intervention. Despite offering reliable enhancements through explainable approaches, these methods suffer from high false detection rates and lack automation, as current techniques often require manual inspection by experts who analyze pre-computed spectral ratio products. This reliance on human analysis makes the process labor-intensive and inefficient. Additionally, these methods are vulnerable to retrieval artifacts, particularly from surface features mistakenly identified as methane plumes, further exacerbating false detection issues.

From the perspective of methane concentration retrieval, traditional techniques struggle with accurately distinguishing true methane enhancements from background noise and artifacts. The manual processes involved in identifying and masking plumes are time-consuming and prone to inconsistencies and errors, leading to unreliable concentration estimates (Růžička et al., 2023). Moreover, the variability in wind

speed characterization complicates accurately estimating methane point source rates. Effective wind speed must account for vertical averages over the plume extent, yet traditional methods often lack the capability to capture detailed horizontal wind variability across the plume’s scale. This limitation results in less precise source rate estimates, as the methods cannot consistently account for the complex wind dynamics influencing plume dispersion.

Thus, despite advancements in methane detection techniques, traditional methods remain constrained by their dependence on manual intervention. They are susceptible to inaccuracies in methane concentration retrieval and point source rate estimation. These limitations highlight the need for more automated and robust approaches that can effectively handle the intricacies of plume detection and quantification without extensive human oversight.

4. Machine learning approaches for methane applications

With the increasing popularity of ML in the last decade, scientists have recently employed modern ML methods for methane detection and quantification of emission rates. ML approaches, first applied to general computer vision tasks (gain understanding from digital images), are widely applied to the methane domain. As explained in Chapter 3, the classical methods rely on complex and computationally intensive simulations to produce consistent and accurate results. For ML models, less domain expertise and no simulation are needed, which results in higher automation, faster processing, and energy-efficient methane detection. For example, Schuit et al. (2023) employed ML models for faster methane detection for Sentinel 5P at the Netherlands Institute for Space Research (SRON), reducing the overall processing time. In this Chapter, we will review and summarize the ML approaches used for methane plume segmentation and emission rate estimation tasks. In addition, some researchers (e.g. Radman et al. (2023); Si et al. (2024)) have developed methods to estimate the emission rate directly from satellite observations. Some of the models also include wind information, which may substantially increase the uncertainty of the prediction.

The most used ML architecture hereafter is based on CNN and transformer. The fundamental idea for CNN is to use learnable kernels, which will be convolved with the input data in a 2D image-like form. This operation gives the model great flexibility to focus on different properties in a local neighborhood of each pixel (Ronneberger et al., 2015; Gu et al., 2018). Transformers combine multiple attention layers and Multi-Layer Perceptrons (MLP) to learn relationships between the queries (Q) and the keys (K) (Vaswani et al., 2017), resulting in the relationship between all the different pixels. Transformers were applied to text analysis first and to images shortly after (Dosovitskiy et al., 2020).

4.1. Machine Learning methods for plume segmentation

Creating a methane plume mask involves a fundamental computer vision task known as image segmentation, where the objective is to partition an image into dis-

tinct regions corresponding to different classes, in this case, 'plume' and 'no-plume'. Modern approaches in computer vision rely on state-of-the-art models that incorporate attention mechanisms, which form the basis for transformer models. Historically, image segmentation models transitioned from traditional ML classifiers like decision trees and support vector machines to deep learning architectures. Deep learning models such as perceptrons, MLP, CNN, and transformers excel at feature extraction and reasoning, making them well-suited for tasks like image segmentation. Despite the growing application of ML in various remote sensing domains, its utilization remains limited due to challenges such as insufficient annotated training data and the complexities inherent in unsupervised or semi-supervised methods. Still, there has been a recent uptick in adopting ML techniques for methane plume segmentation. However, the volume of research in this area still lags behind other domains within remote sensing, like cloud detection. Cloud detection is a related segmentation task using remote sensing data in which different ML approaches are frequently employed.

This chapter will provide an overview of used datasets and metrics before analyzing different ML approaches.

4.1.1. Datasets for plume segmentation

Many authors produced data for training plume segmentation models by simulating methane plumes and superimposing them into real observations. Some authors put plenty of effort into the manual annotation of the plumes. To provide an overview of which datasets for which mission exist and can be accessed, we consolidated the datasets with some information in Table 4. As shown in this Table, the amount of data is still relatively sparse for deep learning methods, with just three openly available datasets. AVIRIS-NG data has been widely used as this mission provides the most accessible annotated data. Some more datasets could be used for plume segmentation, like Gorroño et al. (2021) providing simulated Sentinel 2 data, but these datasets do not provide a plume mask for ground truth. The EnMAP dataset (Si et al., 2024) consists of all available EnMAP bands that are not sensitive to water vapor or CO₂, resulting in 41 bands. In Table 4, the *Mission* describes the mission names or the instrument in the case of AVIRIS-NG. The *Bands* describe the used bands in the dataset and processing level, sometimes interpolated to a consistent spatial resolution marked in parenthesis. The number of samples is given in the *num samples* column, and the *image size* is provided in the number of pixels. The column *Aug* mentions if this dataset is augmented using techniques like rotation or changes in brightness. The *Access* is grouped into per request (*req*), *open* for free access, and “-” for unknown data access. Whether or not the data has been simulated is stated in *Sim*, and *Ref* describes the reference for further information about the datasets.

4.1.2. Evaluation metrics

The authors using ML for methane plume segmentation employ a variety of metrics, which complicates model comparison. The commonly used metrics are described below (Rainio et al., 2024).

Table 4: Available datasets for Plume segmentation

Mission	Bands	Num samples	Img size	Aug	Access	Sim	Ref
Sentinel 5P	1 (L2)	>1.800	16 x 22	no	req	no	Lauvaux et al. (2022)
Sentinel 2	all (10m, L1)	10.046	200 x 200	no	req	no	Vaughan et al. (2024)
Sentinel 2	all (20m, L1)	1.650.000	128 x 128	no	-	yes	Rouet-Leduc and Hulbert (2024)
AVIRIS-NG	RGB and enhancement	167.825	512 x 512	yes	open	no	Růžička et al. (2023)
AVIRIS-NG	RGB and enhancement	46	23k x 1.5k	no	open	no	Thompson et al. (2017)
AVIRIS-NG	all (L1)	3.961	256 x 256	no	-	no	Kumar et al. (2023)
AVIRIS-NG	all (L1)	7.000	-	no	-	yes	Jongaramrungruang et al. (2022)
GHGSat-C1	1 (L2)	6.870	128 x 128	yes	open	yes	Bruno et al. (2023)
EnMAP	41 (L1) and enhancement	7200	256 x 256	no	-	yes	Si et al. (2024)

$$\begin{aligned}
\text{Accuracy} &= \frac{TP + TN}{TP + TN + FP + FN}; & \text{Precision} &= \frac{TP}{TP + FP}; \\
\text{Recall} &= \frac{TP}{TP + FN}; & \text{IoU} &= \frac{TP}{TP + FP + FN}; & \text{F1} &= 2 * \frac{\text{Precision} * \text{Recall}}{\text{Precision} + \text{Recall}}
\end{aligned} \tag{6}$$

$$FPR = \frac{FP}{FP + TN}; \quad FNR = \frac{FN}{FN + TP}; \tag{7}$$

The used metrics for methane plume segmentation, similar to those employed in cloud detection, are Precision (Schuit et al., 2023; Rouet-Leduc et al., 2023; Vaughan et al., 2024; Groshenry et al., 2022; Kumar et al., 2020), F1-Score (Schuit et al., 2023; Růžička et al., 2023; Groshenry et al., 2022; Kumar et al., 2020; Rouet-Leduc and Hulbert, 2024), Recall (Schuit et al., 2023; Vaughan et al., 2024; Groshenry et al., 2022; Kumar et al., 2020), Accuracy (Schuit et al., 2023; Jongaramrungruang et al., 2022; Vaughan et al., 2024), Intersection over Union (IoU) (Bruno et al., 2023; Groshenry et al., 2022; Kumar et al., 2020), False Positive Rate (FPR) (Rouet-Leduc et al., 2023; Vaughan et al., 2024; Růžička et al., 2023), mean Intersection over Union (mIoU) (Groshenry et al., 2022; Kumar et al., 2023). Single publications also utilized median Average Precision (mAP) (Kumar et al., 2023), Average Precision (AP) (Si et al., 2024) False Negative Rate (FNR) (Vaughan et al., 2024), True Positive Rate (TPR) (Rouet-Leduc et al., 2023), and Area under the Precision-Recall Curve (AUPRC) (Růžička et al., 2023). However, Joyce et al. (2023) did not provide any metric for plume segmentation performance.

While some metrics are available for comparison, difficulties arise when authors present performance graphically for each sample instead of providing averages. Additionally, some authors adjust metrics based on SNR, considering different scenes, while others assume a homogeneous scene and assess algorithms based on emission

rate. Variations in surface characteristics lead to fluctuations in instrument-measured radiance, impacting estimated methane concentrations and emission rates. For the comparability of the various presented models, objective evaluations on standardized benchmark datasets would be needed. A robust comparison of ML models requires extensive datasets with comparable statistics regarding emission rate, albedo, viewing angle, radiance, scenes, wind speed, and other parameters for each sensor. Such datasets would facilitate clear comparisons and enable evaluations across different sensors. Moreover, these datasets could serve as benchmarks for new methods, offering insights into overall performance and comparisons with existing techniques.

4.1.3. Approaches for plume segmentation

We will shortly discuss ML approaches for cloud detection to show a variety of different approaches that could be applied to methane plume segmentation.

For cloud detection, Foga et al. (2017) and Qiu et al. (2019) utilized decision tree models like See5 and Automated Cloud Cover Assessment, yielding commendable performance, albeit with lower accuracy compared to more recent methods. Singular value decomposition was employed by Xie et al. (2017) to generate pertinent features for Support Vector Machines (SVM) while exploring clustering methods such as K-means for grouping satellite images. Probabilistic approaches applied to handcrafted features using a Bayesian classifier were studied by Mahajan and Fataniya (2020), who also compared the results with random forest, fuzzy logic approaches, boosted random forests, and probabilistic latent semantic analysis. However, these methods exhibited inferior performance compared to deep learning and CNN.

Especially the CNN-based U-net architecture (Ronneberger et al., 2015) was widely applied. Enhancements to the U-net model have been proposed by Li et al. (2023), who initially utilized two U-net structures for segmentation, identifying possible cloudy regions and refining the selection through the second U-net. Combination approaches involving CNN and MLP, ensemble methods employing voting mechanisms for pixel classification, and the use of alternative architectures like RS-Net, VGG-16, SegNet, or Pyramid Scene Parsing Network have also been explored Li et al. (2021).

Furthermore, strategies such as superpixel grouping through Simple Linear Iterative Clustering followed by CNN processing for cloud detection were introduced by Xie et al. (2017). Inspired by transformer attention modules, Li et al. (2023) integrated attention modules into the skip-connections of the U-net architecture. Additionally, the Vision Transformer was employed for cloud detection by Zhang et al. (2023). Recent semi-supervised approaches have introduced the Swin Transformer, combined with CNN and multi-head attention mechanisms for cloud detection by Gong et al. (2023).

Various methodologies have been explored in the cloud detection domain, contrasting with methane plume segmentation where CNN models predominate, especially based on the U-net architecture shown in Figure 2. This preference for CNN

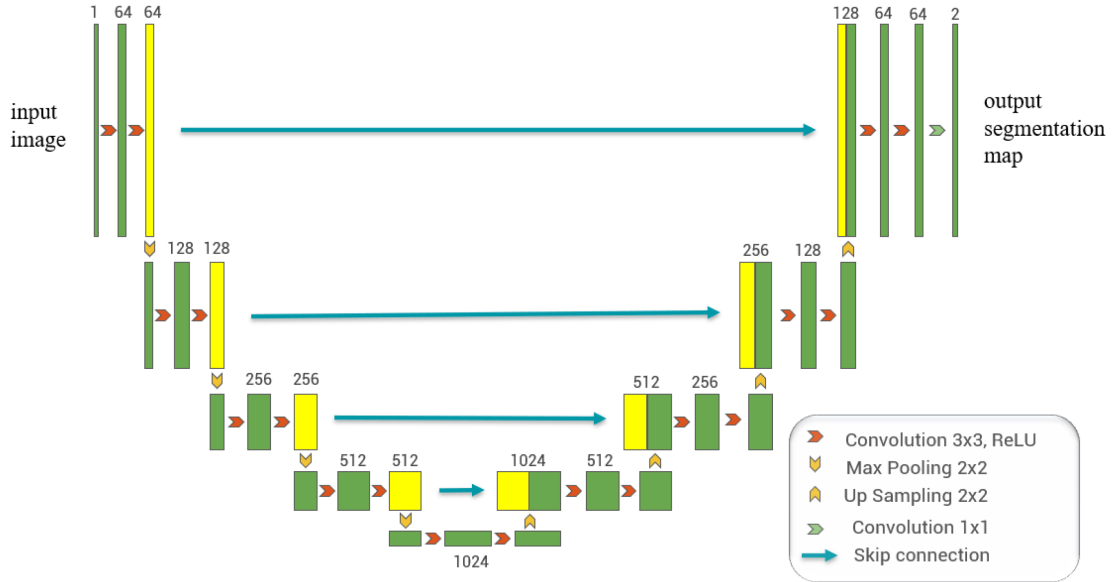


Figure 2: This image by Guo et al. (2020) depicts the U-net architecture of Ronneberger et al. (2015) under a CC-BY license. The U-net architecture has been used in different forms for recent methane plume segmentation approaches. The architecture uses different convolution sizes, reduces the image size first (encoder) to reduce the feature space, and decodes the image (decoder) back to its original shape, additionally providing skip connections for more effective learning.

may stem from their superior performance and ability to retain spatial information, a quality often lost in classifiers like decision trees or SVM (Schuit et al., 2023). Next, we would like to discuss the applied ML approaches for methane plume segmentation.

One smaller ML architecture has been used by Schuit et al. (2023), which employed a CNN encoder (consisting of two CNN layers) with a classification head (comprising two MLP layers) for methane plume segmentation using pre-processed Sentinel 5P observations. The architecture is shown in Figure 3. Their study revealed that deeper networks did not yield improved performance. The authors introduced a plume shape and class activation map (Zhou et al., 2016), along with hand-selected features, into a Support Vector Classifier to discern between real plumes and artifacts through binary classification. Similarly, Finch et al. (2022) employed a similar architecture for Nitrogen oxides (NO_x) plume segmentation in Sentinel 5P data. A slightly larger model has been employed by Jongaramrungruang et al. (2022), who developed Methanet primarily for emission rate estimation but adapted the model’s head to a binary classification of plume presence using 4 convolutional layers with 2 MLP layer trained on simulated AVIRIS-NG data with an accuracy of 90% for emission rate >100 kg/h and 50% for emission rate of 50-60 kg/h.

The next works employ the standard or modified version of the U-net model. The first use of the U-net architecture was by Groshenry et al. (2022), which generated transformed plumes and methane concentration maps from Sentinel 2 to PRISMA

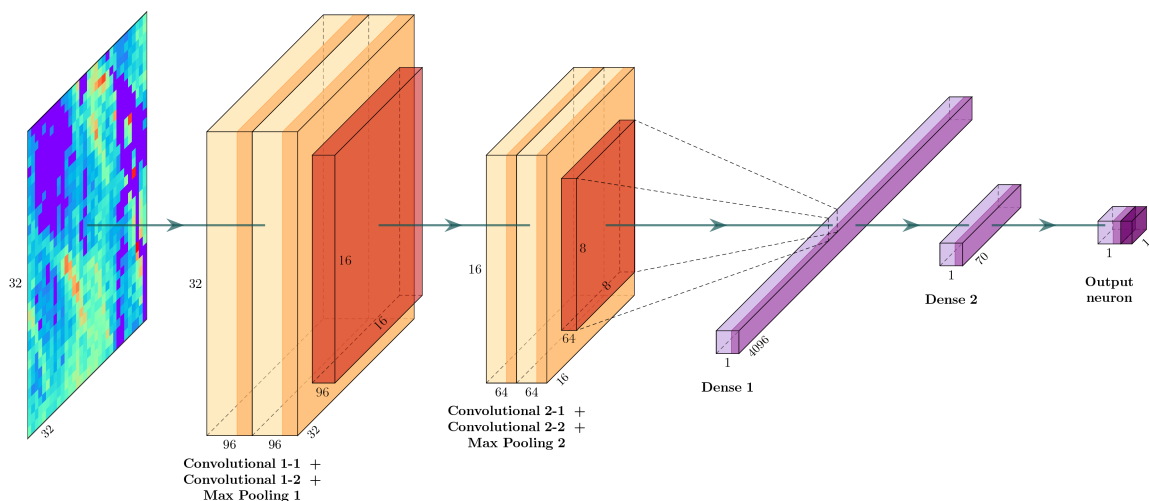


Figure 3: Architecture used by Schuit et al. (2023) under the CC-BY 4.0 license

scenes for training a U-net model. The authors reported that the model trained solely on PRISMA data performed better than the training on Sentinel 2 plumes adapted to the PRISMA images. However, the comparison and transformation of Sentinel 2 plumes into PRISMA scenes is not clearly described. Following the same architecture Bruno et al. (2023) focused on the widely used U-net architecture for GHGSat image segmentation, training the model on simulated plumes superimposed onto GHGSat plume-free observations. They evaluated performance using the Jaccard score (Intersection over Union), resulting in improved results in low background noise scenarios. CH4Net has been introduced by Vaughan et al. (2024), training a 4 Block U-net on hand-annotated Sentinel 2 observations, achieving enhanced performance by integrating all available bands into the model. The authors interpolated the bands to 10m resolution and found improved performance when integrating all bands. Utilizing simulated Gaussian plumes superimposed onto Sentinel 2 images for training, a U-net model has been employed by Rouet-Leduc et al. (2023). They employed all band ratios from two consecutive Sentinel 2 images, interpolated to 20 m resolution, and achieved improved results compared to the MBMP (Varon et al., 2021) (using a threshold) method for low Signal-to-Noise Ratio (SNR). Another model for PRISMA data training a U-net on simulated plumes superimposed onto real observations, incorporating an additional 1x1 convolutional layer with 64 filters for robustness towards anomalies and an auxiliary loss function to address plume class imbalance, has been trained by Joyce et al. (2023).

The U-net architecture and a more sophisticated computer vision model have been used by Ružička et al. (2023). The authors utilized AVIRIS-NG observations with manually annotated plumes and simulated Worldview-3 images for training two different U-net architectures, employing the MobileNet-v2 (Sandler et al., 2018) encoder and the standard U-net decoder for each sensor. The authors provided the methane

enhancement map and RGB images of the scene as input for the model, resulting in lower detection of artifacts and, therefore less false positives. More complex CNN models have been used by Kumar et al. (2020), who used a new approach within plume segmentation by using the ensemble method. The authors used all AVIRIS-NG bands and grouped them for input into matched filters for multiple methane maps. These maps are forwarded into a Mask-RCNN (He et al., 2017), each using the Resnet101 (He et al., 2016) for the backbone model. The backbone has been pre-trained on the Common Objects in Context (COCO) dataset (Lin et al., 2014) and fine-tuned for hyperspectral remote sensing. The output of this ensemble is then fused into an ensemble network (2-layer MLP also using terrain information) for plume segmentation. Within a second work, the Mask-RCNN has been employed by Si et al. (2024) using PRISMA and EnMAP data using simulated plumes. The authors compared the use of raw hyperspectral data with concentration maps and a multi-task model combining two models (Mask R-CNN for plume segmentation and a ResNet-50 for emission rate estimation) trained together. They found increased results when using methane concentration maps and the best results when combining the two models.

So far, all authors have used CNN as a basis model for plume segmentation. However, some authors were able to apply the first transformer model for plume segmentation/detection. Kumar et al. (2023) used a pre-trained detection transformer and pre-trained ResNet (He et al., 2016) model together using AVIRIS-NG observation for plume segmentation and bounding box around the plume. The authors use a spectral feature generator (selector and CNN model backbone) to generate methane plume candidates to be used in a query refiner. Parallel to that, methane-sensitive bands use the CNN backbone for feature generation, which will be embedded for cross-attention between the embedding and the query refiner for the decoder transformer model. The output is used for a pyramid model (2 layer MLP) to generate the bounding box and a mask predictor using the methane-sensitive features, encoded image, and encoded features. The mask predictor consists of the segmentation head of the Detection transformer (DETR) (Carion et al., 2020). Heat maps for each plume will be produced and filtered by a threshold for plume mask generation. The complex architecture is depicted in Figure 4.

The recent work of Rouet-Leduc and Hulbert (2024) built a large dataset using simulated Gaussian plumes superimposed into Sentinel 2 images using the Beer-Lambert law (Ehret et al., 2022) from different countries across the world. The authors then trained a model using a vision transformer encoder and CNN decoder from scratch, following a U-net architecture for pixel-wise binary classification. The trained model provides a low false positive rate, better detection at low SNR compared to MBMP with threshold, and significantly lowered the detection limit of Sentinel 2 down to 200-300 kg/h. The detection limit has been tested on further detected plumes from AVIRIS-NG and Global Airborne Observatory (GAO), labeling a plume as detected if at least 2 consecutive pixels are marked as 'plume', which is not more than 500 m away from the beforehand detected source location. However, it is unclear if

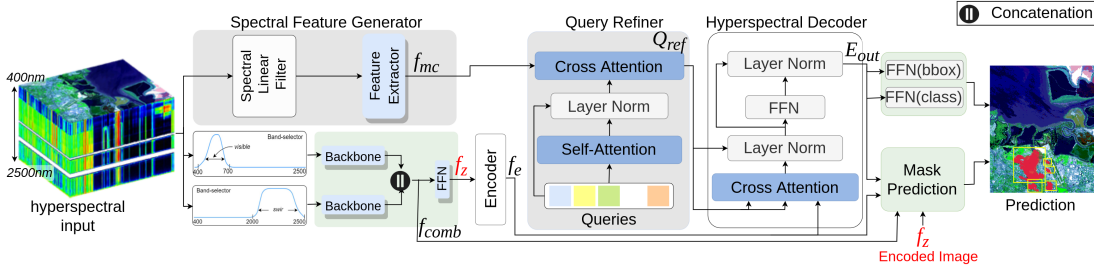


Figure 4: Architecture based on CNN and transformer elements used by Kumar et al. (2023) for plume detection and segmentation under the CC-BY 4.0 License. f_{mc} describes potential CH_4 feature maps, f_{comb} is the combined output of the Backbones using different spectral ranges, f_z is the output of two MLP from f_{comb} , f_e is the feature encoded f_z .

the detected plume pixels are valid pixels of a plume and need further investigation.

In plume segmentation using ML, the prevailing approach typically involves simple or U-net structured CNN, yielding higher accuracy than threshold-based methods. Due to the labor-intensive nature of generating ground truth plume masks from real observations, many authors resort to simulated data tailored to the specific sensor. To approximate real-world conditions, simulated plumes are often overlaid onto actual observations devoid of plumes, capturing realistic background and sensor noise. In contrast to cloud detection, probabilistic approaches for plume segmentation were not prevalent at the time of writing. Performance metrics for methane plume segmentation vary, posing challenges in comparing different methods. Another hurdle is comparing different satellite sensors, such as AVIRIS-NG and Sentinel 2, which exhibit discrepancies in spectral and spatial resolutions and surface characteristics, leading to variations in SNR for identical plumes. Even among studies utilizing the same sensor, such as AVIRIS-NG data (Jongaramrungruang et al., 2022; Ružička et al., 2023; Kumar et al., 2020, 2023), comparability is hindered by the adoption of different metrics, with some studies altering metrics mid-research (Kumar et al., 2020, 2023), further complicating cross-study comparisons.

4.2. Machine Learning methods for emission rate estimation

The task of estimating the emission rate of a particular methane plume is, from an ML perspective, a general image-level regression task. Regression describes the challenge of finding correlations of the given inputs, which could be independent or dependent variables on the desired output. It is commonly the task to minimize the distance between the desired output and the model’s prediction. Next, we will describe the available datasets, metrics, and different ML approaches for emission rate estimation.

4.2.1. Data sets for emission rate estimation

The ML approaches for emission rate estimation rely on supervised training and, therefore, on many ground truth data. For this reason, many authors relied on

simulated plumes superimposed on the specific observation. Table 5 lists the used datasets for the ML approaches and further available datasets. In addition to the Table, different authors used plume simulations to find a suitable effective wind speed for the IME method or for validating sensors. However, these datasets are limited to specific areas and contain a small amount of samples in most cases, but the generated synthetic dataset is often not further described or released. For example, this has been done, e.g., by Roger et al. (2023a).

In Table 5, the *Mission* is named or the instrument in the case of AVIRIS-NG. The *Bands* represent the number of used bands in the dataset and processing level. If all available channels of the satellite are provided, the number of bands is set to “all”. The number of samples and different scenes is given in the *samples* column, and the *image size* is provided in the number of pixels. The column *Aug* mentions if this dataset is augmented using techniques like rotation or changes in brightness. Next, the *minimum and maximum used emissions* from the simulation in kg/h is described. Accounting for the different wind speeds, the *Wind* column provides the modeled speeds. The *Access* is grouped into per request “req”, open for free access and no for no public access. *Ref* describes the reference for further information about the datasets and “-” describes missing values.

Table 5: Available datasets for emission rate estimation providing simulated ground truth values

Mission	Bands	Samples (Scenes)	Img size	Aug	Min / Max emission (kg/h)	Wind m/s	Access	Ref
Sentinel 2	1 (L2)	7000 3	100x100	no	5k 30k	1-10	req	Radman et al. (2023)
Sentinel 2	all (L1)	1345 3	75x75 (to 20m)	no	500 50k	3.5	open	Gorroño et al. (2021)
PRISMA	all (L1)	9700 36	256x256	no	100 10k	1-9	open	Joyce et al. (2023)
GHGSat-C1	1 (L2)	6870 28	128x128	yes	500 2k	3-9	open	Bruno et al. (2023)
AVIRIS-NG	all (L1)	7000 -	300x300	no	0 2k	0-12	no	Jongaramrungruang et al. (2022)
WorldView3	all (L1)	- 3	406x406	no	100 3k	3.5	req	Sánchez-García et al. (2022)
Sentinel 2	all (L1)	- 700	406x406 (to 20m)	no	100 3k	3.5	req	Rouet-Leduc et al. (2023)
EnMAP	42 (L1)	7200 1	256 x 256	no	500 2000	1-10	-	Si et al. (2024)

4.2.2. Evaluation metrics

For estimating emission rates, methods can only be compared effectively if simulated plumes are utilized to establish a ground truth for evaluation. Consequently, all authors employing ML approaches for emission rate estimation have relied on simulated plumes. Some authors have conducted small-scale controlled emission experiments to validate existing methods and generate ground truth, particularly for

AVIRIS-NG or other flight campaigns. Recently, Sherwin et al. (2024) conducted a single-blind evaluation of different satellite sensors. They synchronized controlled emissions with satellite overpasses and measured the emitted gas, resulting in multiple satellite images. Although these images cannot be directly used for ML or deep learning approaches, as they result in 2 to 5 images from different satellites, they could be used to validate trained models.

The widely used metrics for regression, in general, are the Mean Absolute Percentage Error (MAPE), RMSE, and Pearson correlation coefficient (R) described below (Naser and Alavi, 2023).

The MAPE is defined as

$$MAPE = \frac{100}{n} \sum_{i=1}^n \left| \frac{y_i - \hat{y}_i}{y_i} \right|, \quad (8)$$

where n is the number of data points, y_i is the i -th value, \hat{y}_i describes the i -th prediction of the model.

$$RMSE = \sqrt{\frac{1}{n} \sum_{i=1}^n (y_i - \hat{y}_i)^2}, \quad (9)$$

where y_i , \hat{y}_i are the same values as above for the MAPE.

The Pearson correlation coefficient is defined as (Rainio et al., 2024):

$$R = \frac{\sum_{i=1}^n (x_i - \bar{x})(y_i - \bar{y})}{\sqrt{\sum_{i=1}^n (x_i - \bar{x})^2 \sum_{i=1}^n (y_i - \bar{y})^2}}, \quad (10)$$

where the data points are describes as x_i and y_i and \bar{x} and \bar{y} are the respective means of the data.

For comparing the efficacy of different models, authors typically rely on MAPE (Jongaramrungruang et al., 2022; Radman et al., 2023; Joyce et al., 2023). Radman et al. (2023) additionally included multiple metrics such as RMSE and Pearson correlation coefficient. Similar Si et al. (2024) measured the performance by the RMSE and the Mean Absolute Error (MAE). However, Bruno et al. (2023) did not provide any performance metrics. Moreover, Bruno et al. (2023) and Joyce et al. (2023) presented performance results in plots, further constraining direct comparison.

Due to differences in datasets, simulations, and atmospheric parameters, the metrics used across studies remain non-comparable, akin to challenges encountered in plume segmentation tasks. Harmonizing datasets, as described in Chapter 4.1, would be essential for facilitating meaningful comparisons in this task.

4.2.3. Approaches for emission rate estimation

Within the field of computer vision, a common regression task would be the depth estimation of an image. In this domain, the best-performing models use specialized

convolutions, such as fast Fourier convolutions (Berenguel-Baeta et al., 2023) or attentively combined dilated convolutions (Zhuang et al., 2022) or are based on transformer architecture or a combination of CNN and transformer (Junayed et al., 2022). Typical metrics for comparison are Root mean squared Error (RMSE) or the Absolute Relative Error (ARE) shown in Equation 11 (Hodson, 2022),

$$\text{RMSE} = \sqrt{\frac{1}{n} \sum_{i=1}^n (y_i - \hat{y}_i)^2}, \quad \text{ARE} = \frac{|y_i - \hat{y}_i|}{|y_i|} \quad (11)$$

where n is the number of data points, y_i is the i -th value, \hat{y}_i describes the i -th prediction of the model.

For remote sensing regression tasks, finding a domain similar to emission rate estimation adopting various ML approaches is difficult. One regression domain is to determine soil parameters using ML approaches Multiple Linear Regression (MLR), Random forest regression, SVM for regression or Stochastic gradient boosting (Forkuor et al., 2017). Generally, the more complex ML approaches show improved performance to MLR using RMSE (Forkuor et al., 2017). Within the global land surface temperature domain, MLP has been used (Cifuentes et al., 2020). For estimating land surface temperature, CNN-based models have been used by Tan et al. (2019) or even 3D-CNN by Fu et al. (2022), providing promising results.

Like plume segmentation, the different ML approaches for emission rate estimation are scarce. The various ML classifiers or transformers have not been tested for now. Some of the mentioned emission rate methods (see Chapter 3.2) rely on wind speed and direction.

Wind information is a crucial parameter for the traditional approaches, while some ML approaches do not contain any wind information. Wind information for each pixel results from weather forecasts on a much coarser grid most of the time, as accurate wind data is often unavailable. ERA5, the weather prediction model from the European Centre for Medium-Range Weather Forecasts (ECMWF), provides worldwide weather data on a 9x9 km grid (using ERA5-Land). In contrast, the Global Forecast System (GFS) of the American National Weather Service (NWS) provides a 28x28 km resolution. As the grid information is more coarse than the pixel size of most satellites, it results in uncertainty, while the information itself is a prediction that includes uncertainty and may vary for different locations. Therefore, many authors assume an uncertainty in wind information of 50% (Roger et al., 2024; Joyce et al., 2023; Guanter et al., 2021). High uncertainties arise in emission rate estimation due to varying boundary layer conditions like turbulence and wind speed, spectral interferences, and the sensitivity of the flux inversion to complex plume structures. Using traditional approaches, the overall uncertainties can be up to 100% for individual plumes (Duren et al., 2019). It can be observed that some models without wind data provide a lower uncertainty. Whether or not the inclusion of wind information into the model provides benefits or impacts the uncertainty of the model

will be mentioned by the different authors and summarized.

The first deep learning approach for emission rate estimation has been implemented by Jongaramrungruang et al. (2022). The authors tested the same model used for plume segmentation for regression tasks, achieving favorable results across wind speeds and emission rates, even without explicit integration of wind information. They identified an emission rate limit of approximately 50 kg/h for their model, which reduced error ranges from 15-65% using the traditional IME method to 21% without wind information. Instead of using the enhancement maps as the only input, Joyce et al. (2023) employed multiple CNN models for plume segmentation, methane concentration estimation, and binary classification (presence of plume in the image) as inputs for an emission rate CNN model. Their model, comprising 8 convolutional layers, achieved a median error of 25%, compared to approximately 50% using traditional methods. Utilizing multiple models for intermediate steps resulted in improved performance compared to Jongaramrungruang et al. (2022). Compared to these models Bruno et al. (2023) conducted a comparative study between a CNN-based model and the IME method for emission rate estimation using simulated plumes in GHGSat images. While the authors did not explicitly describe the architecture of their model, examination of a provided Jupyter notebook revealed a model comprising 2 convolutional layers, 4 down convolutional layers, and a regression head (comprising 2 MLP layers and Rectified Linear Units (Bruno (2023)) which is similar to the architecture in Figure 3. They observed a smoothing bias in their model, which tended to overestimate low emission rates and underestimate large emission rates, similar to findings by Jongaramrungruang et al. (2022) and Joyce et al. (2023). However, the CNN model exhibited greater robustness due to lower uncertainty. However, wind speed from the simulation has been integrated, providing no error in wind information, whereas wind direction integration had negligible effects. Notably, errors in wind prediction dominated when wind speeds were below 4 m/s, while plume mask errors dominated for higher wind speeds. Emission rate estimation for Sentinel 2 has been conducted by Radman et al. (2023), which employed simulated plumes in observations to estimate emission rates using various deep learning methods, including CNN-based models and a transformer model (He et al., 2016; Szegedy et al., 2015; Simonyan and Zisserman, 2014; Huang et al., 2018; Tan and Le, 2021; Liu et al., 2021). These models, operating without wind information, consistently underestimated larger emission rates, with CNN approaches showing stronger underestimation. The authors compared models trained with random initialization, pre-trained on ImageNet (Deng et al., 2009), and fine-tuned on this task, demonstrating the efficiency of fine-tuning pre-trained models. They identified CNN models as the most suitable for emission rate estimation, outperforming IME and MethaNet of Jongaramrungruang et al. (2022). Additionally, using pre-trained AlexNet and ResNet-50 (fine-tuned to emission rate estimation) results in better estimations than IME (Si et al., 2024). The authors found a better performance of the ResNet-50 model for the single task of emission rate estimation compared to a multi-task model for the plume segmentation and the emission rate

estimation.

The works of the aforementioned authors demonstrated improved performance compared to IME using CNN. As for plume segmentation, CNN dominates this task, with few alternative approaches explored. Radman et al. (2023) compared transformer models to various CNN models and found superior performance in CNN. However, all ML methods tended to underestimate large emissions, albeit to varying degrees. This raises whether alternative ML architectures or approaches could yield improvements. Notably, unlike IME, current ML models do not integrate wind information for emission rate estimation, reducing uncertainty. The assumed mean absolute error of the wind speed is $\pm 50\%$ (Roger et al. (2024); Joyce et al. (2023); Guanter et al. (2021)). Investigating the impact of integrating wind information into ML models warrants further research. Additionally, the authors used two different inputs for the ML models: either only the enhancement maps like Jongaramrungruang et al. (2022); Radman et al. (2023) or the enhancement map together with a plume mask used by Joyce et al. (2023); Bruno et al. (2023). As a realistic comparison is impossible, this would be an additional topic to be investigated, which could be compared using an aligned dataset testing both approaches.

5. Discussion and Outlook

Recent studies and models utilizing ML for methane-related tasks have demonstrated significant advantages, including enhanced accuracy, faster execution times, reduced uncertainty, and increased automation. Most of these ML-based works have been published within the past five years. This trend underscores the growing interest and application of ML in methane-related tasks. Furthermore, the frequent inclusion of the term “automatic” in the titles of these works indicates a strong desire to automate methane detection processes.

Current ML models have successfully reduced human intervention for designing specific features, adjusting thresholds, or conducting radiative transfer simulations, promoting a more automated approach. However, manual checks are still required to verify whether the detected plume is an artifact or a genuine plume and whether the plume segmentation was successful.

One potential solution to this challenge could be the application of explainable AI, which would provide insights into the model’s decisions and foster greater trust in its performance and outcomes. This could be used to investigate which parameters or areas the model focuses on and to fine-tune the focus for better prediction. This could lower the necessary manual investigation.

Combining different models using ensemble methods could further minimize false detections and reduce human involvement. The methodology of Pandey et al. (2023) proposes a rapid and global methane detection system, employing an array of satellites to precisely locate emission sources. This system utilizes satellites with high temporal resolution but coarse spatial resolution and progressively refines the location using

satellites with finer spatial resolution. While this system is an excellent foundation, it requires manual intervention at each stage. Integrating ML and data fusion techniques could automate this process, accelerating the development of a continuous monitoring system for large-scale emissions. However, the high detection limits of satellites with coarse spatial resolution present a constraint that needs to be addressed.

Looking ahead, we expect the development of more models, potentially featuring complex architectures inspired by applications in the computer vision domain. However, these complex models usually require more training data due to their increased number of trainable parameters. The variety of models could show which kind of model works best in specific domains when providing benchmark datasets. This shows the downside of ML needing large amounts of training data to train complex models and to compare models. In parallel to the development of new models, we also expect a stronger focus on simulated and curated datasets for methane detection. Similar methodology from benchmark datasets within computer vision could be applied to methane tasks for comparison.

The uncertainty of ML models and the influence of input parameters (e.g. wind speed) is still unclear and needs in-depth analysis. This analysis might research further benefits and limitations of ML approaches with respect to specific domains, areas, or situations. The investigation of uncertainty could distinguish downsides for specific use cases, allowing for the selection of appropriate models for particular scenarios that are unknown so far.

The models mentioned here are purely ML or physics based. Physics-informed or hybrid ML models combining physics and ML could improve the overall prediction performance. These models may combine information from image analysis and physical approaches like IME for a consistent prediction.

For plume segmentation, existing ML methodologies offer substantial advantages over traditional threshold methods, an advantage that may further increase in the future. ML techniques excel in distinguishing between plumes and background noise, an area that could see further enhancement through the application of diffusion models. These models can potentially learn and reduce the noise in real-world data, thereby improving plume segmentation.

Estimating emission rates poses a significant challenge due to the scarcity of ground truth samples and the potential disparity between simulations and real-world data. While more controlled-release experiments would yield additional data, they also pose environmental risks due to the artificial emissions they produce. Given the limited data, these controlled emissions could be more effectively used for model validation rather than training. In this context, further investigation is needed to determine whether compute-intensive physical simulations are necessary to maintain physical consistency within the simulations or if the Gaussian plumes used by Rouet-Leduc and Hulbert (2024) are sufficient for training, given their rapid and voluminous generation. Another potential approach involves creating a surrogate model of the physical plume simulation, possibly through a physically informed ML model, Gen-

erative Adversarial Networks, or generative diffusion models. This would enable the accurate and rapid generation of plumes to create large datasets. The same simulated plume parameters could also be utilized across different datasets, considering different spatial resolutions as other satellite specifications are incorporated at a later stage. Using the same plumes for different sensors could provide a comparative advantage.

The recent release of a legislative act by the EU Parliament aimed at reducing methane emissions underscores the progress being made in combating these emissions (European Commission, 2019). This Methane Act mandates that oil and gas producers monitor their assets and report emissions, fostering fast detection and mitigation. This legislation could potentially boost the use of additional satellites for methane detection, thereby enhancing prediction accuracy, expanding observational coverage, and increasing the frequency of monitoring. Since most satellites have an expected lifespan of approximately seven years (as per the average in Table 1), collecting large real-world datasets of methane plumes globally might not be feasible. However, satellite-specific data simulation could develop a dataset before the satellite’s launch, allowing for extended testing on real-world data.

This work focused on the application of methane, even though the tasks and challenges are similar to other Molecules like CO_2 or NO_x . Further investigation could be done to analyse the synergies between these domains. A potential benefit of cross-domain approaches may be the training of a segmentation model to general plume structure (e.g. CO_2 plumes) and fine-tune the model for methane segmentation. However, there could be some specific differences that are hard to overcome for a cross-domain model.

6. Conclusion

In this study, we compiled existing and future systems for methane detection and compared traditional physics-based approaches with ML techniques. We explored various multi- and hyperspectral satellite systems capable of methane detection, ranging from coarse resolution with global coverage to fine resolution for local areas. The recent launch of MethaneSat focuses on an intermediate step between coarse area flux mappers and point source mappers. Trends indicate a shift toward specialized greenhouse gas instruments using a few bands or generalized instruments with hyperspectral capabilities. Future systems will focus on high spectral resolution instead of lower GSD, aiming to reduce the detection threshold for even smaller methane plumes. The most common methods for methane plume segmentation and emission rate quantification remain traditional physical approaches. Among these, the band ratio technique for multispectral instruments or the matched filter approach for hyperspectral instruments provides an effective and reliable method for methane enhancement calculations. Plume segmentation predominantly relies on thresholding approaches, with innovative methods proposed by researchers such as using a connection of low and high thresholds like by Watine-Guiu et al. (2023) or connected amount

of plume pixel by Schuit et al. (2023). The IME method for estimating emission rates considers critical physical parameters such as dissipation and diffusion. It offers an efficient and easily computable algorithm. However, to effectively utilize IME, one must perform various simulations to approximate the important factor of effective wind speed (U_{eff}).

ML has demonstrated advantages in both detection and emission rate estimation tasks. Existing research indicates improved performance for multiple satellites and airborne sensors using multi- and hyperspectral imagery. These models heavily rely on CNN and architectures like the U-net. The work of Rouet-Leduc and Hulbert (2024) opens a new path stating that the detection threshold can be drastically improved with a transformer-CNN-based model and a large training dataset. However, it is unclear if the performance can be generalized. Interestingly, some authors observed a smoothing effect in emission rate estimation in the validation dataset, leading to overestimating low and underestimating high emission rates. This smoothing effect results, among other effects, from strong weights of outliers/extremes of the RMSE function (Naser and Alavi, 2023). Addressing this issue requires different loss functions or data and a thorough comparison of different deep-learning approaches, which remains relatively unexplored for methane detection.

Recent efforts have been made to create ML-ready datasets for AVIRIS-NG and Sentinel 2 to facilitate model comparison. However, the AVIRIS-NG dataset has limitations as it provides the methane enhancement map and RGB channels for each sample rather than the hyperspectral data used by other studies (e.g., Kumar et al. (2023); Joyce et al. (2023)). While the simulated Sentinel 2 dataset by Radman et al. (2023) could serve as a baseline, it is not openly available. Additionally, other available datasets offer limited training data and a small variety of scenes and backgrounds, constraining their use for training deep learning models. The main challenge for ML models remains the scarcity of training samples, especially when dealing with satellite data for estimating emission rates. Generating accurate real-world ground truth data is both expensive and difficult to manage. Ground truth data can either be estimated and compared using different algorithms, as demonstrated in the work by Růžička et al. (2023), or based on simulations, as explored in the research of Radman et al. (2023). However, models trained on simulated data need further investigation on larger datasets, as many studies have only tested them on a limited number of samples. One potential solution is to provide precise ground truth through simulations and supplement it with a large real-world test set to evaluate model performance on actual data.

Models should be comparable across different sensors using common objective performance metrics. We anticipate increased adoption of ML in this domain, resulting in diverse models, exploration of different architectures, and potentially task and domain-agnostic approaches. Additionally, there is a growing interest in foundation models in the ML community. These models could be effectively applied (Zhu et al., 2024), typically in a label-efficient manner, when specifically fine-tuned for methane

detection.

Acknowledgments

Author Contributions

Conceptualization – ET. Methods – ET, SZ (traditional approaches). Writing (original draft) – ET. Writing (review and editing) – all authors. Supervision – AK, KH, RS, XZ. Project administration – ET.

Funding

This research has been enabled by OHB Digital Connect GmbH (also involved in the decision to submit the article for publication) and selected via the Open Space Innovation Platform (<https://ideas.esa.int>) as a Co-Sponsored Research Agreement and carried out under the Discovery programme of, and funded by, the European Space Agency.

Conflicts of Interest

The authors declare that there is no conflict of interest regarding the publication of this article.

References

- Berenguel-Baeta, B., Bermudez-Cameo, J., Guerrero, J.J., 2023. Fredsnet: Joint monocular depth and semantic segmentation with fast fourier convolutions from single panoramas, in: 2023 IEEE International Conference on Robotics and Automation (ICRA), IEEE. URL: <http://dx.doi.org/10.1109/ICRA48891.2023.10161142>, doi:10.1109/icra48891.2023.10161142.
- Brenny, B., Day, J., de Goeij, B., Palombo, E., Ouwerkerk, B., Koc, N.A., Bell, A., Leemhuis, A., Paskeviciute, A., Buisset, C., et al., 2023. Development of spectrometers for the tango greenhouse gas monitoring missions, in: International Conference on Space Optics—ICSO 2022, SPIE. pp. 767–777.
- Bruno, J., 2023. U-Plume Training Data. URL: <https://doi.org/10.7910/DVN/YFRQU4>, doi:10.7910/DVN/YFRQU4.
- Bruno, J., Jervis, D., Varon, D., Jacob, D., 2023. U-plume: Automated algorithm for plume detection and source quantification by satellite point-source imagers. *EGUsphere* 2023, 1–24.
- Buchwitz, M., Reuter, M., Schneising, O., Boesch, H., Guerlet, S., Dils, B., Aben, I., Armante, R., Bergamaschi, P., Blumenstock, T., et al., 2015. The greenhouse gas climate change initiative (ghg-cci): Comparison and quality assessment of near-surface-sensitive satellite-derived co2 and ch4 global data sets. *Remote Sensing of Environment* 162, 344–362.

- Candiani, G., Tagliabue, G., Panigada, C., Verrelst, J., Picchi, V., Rivera Caicedo, J.P., Boschetti, M., 2022. Evaluation of hybrid models to estimate chlorophyll and nitrogen content of maize crops in the framework of the future chime mission. *Remote sensing* 14, 1792.
- Carion, N., Massa, F., Synnaeve, G., Usunier, N., Kirillov, A., Zagoruyko, S., 2020. End-to-end object detection with transformers, in: *European conference on computer vision*, Springer. pp. 213–229.
- CEOS, 2024a. CEOS gho hyperspectral imager. <https://database.eohandbook.com/database/instrumentsummary.aspx?instrumentID=1935>. Accessed: 2024-03-12.
- CEOS, 2024b. CEOS instrument summary - lashis. <https://database.eohandbook.com/database/instrumentsummary.aspx?instrumentID=1925>. Accessed: 2024-06-04.
- CEOS, 2024c. CEOS instrument summary - ss. <https://database.eohandbook.com/database/instrumentsummary.aspx?instrumentID=1936>. Accessed: 2024-06-04.
- Chabrillat, S., Guanter, L., Kaufmann, H., Förster, S., Beamish, A., Brosinsky, A., Wulf, H., Asadzadeh, S., Bochow, M., Bohn, N., et al., 2022. Enmap science plan, (enmap technical report) .
- Chen, Y., Sherwin, E.D., Berman, E.S., Jones, B.B., Gordon, M.P., Wetherley, E.B., Kort, E.A., Brandt, A.R., 2022. Quantifying regional methane emissions in the new mexico permian basin with a comprehensive aerial survey. *Environmental science & technology* 56, 4317–4323.
- Chulakadabba, A., Sargent, M., Lauvaux, T., Benmergui, J.S., Franklin, J.E., Chan Miller, C., Wilzewski, J.S., Roche, S., Conway, E., Souri, A.H., et al., 2023. Methane point source quantification using methaneair: a new airborne imaging spectrometer. *Atmospheric Measurement Techniques* 16, 5771–5785.
- Cifuentes, J., Marulanda, G., Bello, A., Reneses, J., 2020. Air temperature forecasting using machine learning techniques: a review. *Energies* 13, 4215.
- Cogliati, S., Sarti, F., Chiarantini, L., Cosi, M., Lorusso, R., Lopinto, E., Miglietta, F., Genesio, L., Guanter, L., Damm, A., et al., 2021. The prisma imaging spectroscopy mission: Overview and first performance analysis. *Remote sensing of environment* 262, 112499.
- Coleman, R.W., Brodrick, P., Chadwick, K.D., Chlus, A., Eastwood, M., Elder, C., Fahlen, J., Gomezbeltran, S., Hopkins, F., Thompson, D., et al., 2024. Quantification of CH₄ Emissions from the EMIT and AVIRIS-3 Imaging Spectrometers. Technical Report. Copernicus Meetings.

- Cusworth, D.H., Duren, R.M., Thorpe, A.K., Olson-Duvall, W., Heckler, J., Chapman, J.W., Eastwood, M.L., Helmlinger, M.C., Green, R.O., Asner, G.P., et al., 2021. Intermittency of large methane emitters in the permian basin. *Environmental Science & Technology Letters* 8, 567–573.
- Cusworth, D.H., Jacob, D.J., Varon, D.J., Chan Miller, C., Liu, X., Chance, K., Thorpe, A.K., Duren, R.M., Miller, C.E., Thompson, D.R., et al., 2019. Potential of next-generation imaging spectrometers to detect and quantify methane point sources from space. *Atmospheric Measurement Techniques* 12, 5655–5668.
- Deng, J., Dong, W., Socher, R., Li, L.J., Li, K., Fei-Fei, L., 2009. Imagenet: A large-scale hierarchical image database, in: 2009 IEEE conference on computer vision and pattern recognition, Ieee. pp. 248–255.
- Donlon, C., Berruti, B., Buongiorno, A., Ferreira, M.H., Féménias, P., Frerick, J., Goryl, P., Klein, U., Laur, H., Mavrocordatos, C., et al., 2012. The global monitoring for environment and security (gmes) sentinel-3 mission. *Remote Sensing of Environment* 120, 37–57.
- Dosovitskiy, A., Beyer, L., Kolesnikov, A., Weissenborn, D., Zhai, X., Unterthiner, T., Dehghani, M., Minderer, M., Heigold, G., Gelly, S., et al., 2020. An image is worth 16x16 words: Transformers for image recognition at scale. *arXiv preprint arXiv:2010.11929* .
- Dubovik, O., Li, Z., Mishchenko, M.I., Tanré, D., Karol, Y., Bojkov, B., Cairns, B., Diner, D.J., Espinosa, W.R., Goloub, P., et al., 2019. Polarimetric remote sensing of atmospheric aerosols: Instruments, methodologies, results, and perspectives. *Journal of Quantitative Spectroscopy and Radiative Transfer* 224, 474–511.
- Duren, R., Cusworth, D., Ayasse, A., Herner, J., Thorpe, A., Falk, M., Heckler, J., Guido, J., Giuliano, P., Chapman, J., et al., 2021. Carbon mapper: on-orbit performance predictions and airborne prototyping, in: AGU Fall Meeting Abstracts, pp. A53F–05.
- Duren, R.M., Thorpe, A.K., Foster, K.T., Rafiq, T., Hopkins, F.M., Yadav, V., Bue, B.D., Thompson, D.R., Conley, S., Colombi, N.K., et al., 2019. California’s methane super-emitters. *Nature* 575, 180–184.
- Ehret, G., Bousquet, P., Pierangelo, C., Alpers, M., Millet, B., Abshire, J.B., Bovensmann, H., Burrows, J.P., Chevallier, F., Ciais, P., et al., 2017. Merlin: A french-german space lidar mission dedicated to atmospheric methane. *Remote Sensing* 9, 1052.
- Ehret, T., De Truchis, A., Mazzolini, M., Morel, J.M., D’aspremont, A., Lauvaux, T., Duren, R., Cusworth, D., Facciolo, G., 2022. Global tracking and quantification of

- oil and gas methane emissions from recurrent sentinel-2 imagery. *Environmental science & technology* 56, 10517–10529.
- EO Portal, 2016. EO Portal microcarb (carbon dioxide monitoring mission). <https://www.eoportal.org/satellite-missions/microcarb>. Accessed: 2024-06-04.
- EO Portal, 2024. EO Portal geisat constellation. <https://www.eoportal.org/satellite-missions/geisat-constellation>. Accessed: 2024-03-12.
- Etminan, M., Myhre, G., Highwood, E.J., Shine, K.P., 2016. Radiative forcing of carbon dioxide, methane, and nitrous oxide: A significant revision of the methane radiative forcing. *Geophysical Research Letters* 43, 12–614.
- European Commission, 2019. Proposal for a regulation of the european parliament and of the council on methane emissions reduction in the energy sector and amending regulation (eu) 2019/942, european commission, directorate-general for energy, 2021.
- European Parliament WG, 2021. Commission staff working document impact assessment report accompanying the proposal for a regulation of the european parliament and of the council on methane emissions reduction in the energy sector and amending regulation (eu) 2019/942 swd/2021/459 final, 2021.
- Finch, D.P., Palmer, P.I., Zhang, T., 2022. Automated detection of atmospheric no₂ plumes from satellite data: a tool to help infer anthropogenic combustion emissions. *Atmospheric Measurement Techniques* 15, 721–733.
- Fletcher, K., 2012a. SENTINEL 2: ESA’s Optical High-Resolution Mission for GMES Operational Services (ESA SP-1322/2 March 2012). European Space Agency.
- Fletcher, K., 2012b. Sentinel-3: ESA’s Global Land and Ocean Mission for GMES Operational Services (ESA SP-1322/3, October 2012). European Space Agency.
- Fletcher, K., 2016. Sentinel-5 Precursor: ESA’s Atmospheric Chemistry and Pollution-Monitoring Mission (ESA SP-1332, January 2016). European Space Agency.
- Foga, S., Scaramuzza, P.L., Guo, S., Zhu, Z., Dilley Jr, R.D., Beckmann, T., Schmidt, G.L., Dwyer, J.L., Hughes, M.J., Laue, B., 2017. Cloud detection algorithm comparison and validation for operational landsat data products. *Remote sensing of environment* 194, 379–390.
- Foote, M.D., Dennison, P.E., Thorpe, A.K., Thompson, D.R., Jongaramrungruang, S., Frankenberg, C., Joshi, S.C., 2020. Fast and accurate retrieval of methane concentration from imaging spectrometer data using sparsity prior. *IEEE Transactions on Geoscience and Remote Sensing* 58, 6480–6492.

- Forkuor, G., Hounkpatin, O.K., Welp, G., Thiel, M., 2017. High resolution mapping of soil properties using remote sensing variables in south-western burkina faso: a comparison of machine learning and multiple linear regression models. *PloS one* 12, e0170478.
- Frankenberg, C., Platt, U., Wagner, T., 2005. Iterative maximum a posteriori (imap)-doas for retrieval of strongly absorbing trace gases: Model studies for ch 4 and co 2 retrieval from near infrared spectra of sciamachy onboard envisat. *Atmospheric Chemistry and Physics* 5, 9–22.
- Frankenberg, C., Thorpe, A.K., Thompson, D.R., Hulley, G., Kort, E.A., Vance, N., Borchardt, J., Krings, T., Gerilowski, K., Sweeney, C., et al., 2016. Airborne methane remote measurements reveal heavy-tail flux distribution in four corners region. *Proceedings of the national academy of sciences* 113, 9734–9739.
- Fu, H., Shao, Z., Fu, P., Huang, X., Cheng, T., Fan, Y., 2022. Combining atc and 3d-cnn for reconstructing spatially and temporally continuous land surface temperature. *International Journal of Applied Earth Observation and Geoinformation* 108, 102733.
- Gauthier, J.F., 2021. The importance of matching needs to satellite system capability when monitoring methane emissions from space, in: 2021 IEEE International Geoscience and Remote Sensing Symposium IGARSS, IEEE. pp. 687–690.
- Ge, X., Ding, J., Teng, D., Xie, B., Zhang, X., Wang, J., Han, L., Bao, Q., Wang, J., 2022. Exploring the capability of gaofen-5 hyperspectral data for assessing soil salinity risks. *International Journal of Applied Earth Observation and Geoinformation* 112, 102969.
- Gong, C., Long, T., Yin, R., Jiao, W., Wang, G., 2023. A hybrid algorithm with swin transformer and convolution for cloud detection. *Remote Sensing* 15, 5264.
- Gorroño, J., Varon, D.J., Irakulis-Loitxate, I., Guanter, L., 2023. Understanding the potential of sentinel-2 for monitoring methane point emissions. *Atmospheric Measurement Techniques* 16, 89–107.
- Gorroño, J., Varon, D., Irakulis-Loitxate, I., Guanter, L., 2021. Sentinel 2 L1C products with simulated methane plumes (S2CH4). URL: <https://doi.org/10.7910/DVN/KRNPEH>, doi:10.7910/DVN/KRNPEH.
- Green, R.O., Schaepman, M.E., Mouroulis, P., Geier, S., Shaw, L., Hueini, A., Bernas, M., McKinley, I., Smith, C., Wehbe, R., et al., 2022. Airborne visible/infrared imaging spectrometer 3 (aviris-3), in: 2022 IEEE Aerospace Conference (AERO), IEEE. pp. 1–10.

- Groshenry, A., Giron, C., Lauvaux, T., d'Aspremont, A., Ehret, T., 2022. Detecting methane plumes using prisma: Deep learning model and data augmentation. arXiv preprint arXiv:2211.15429 .
- Gu, J., Wang, Z., Kuen, J., Ma, L., Shahroudy, A., Shuai, B., Liu, T., Wang, X., Wang, G., Cai, J., et al., 2018. Recent advances in convolutional neural networks. *Pattern recognition* 77, 354–377.
- Guanter, L., Irakulis-Loitxate, I., Gorroño, J., Sánchez-García, E., Cusworth, D.H., Varon, D.J., Cogliati, S., Colombo, R., 2021. Mapping methane point emissions with the prisma spaceborne imaging spectrometer. *Remote Sensing of Environment* 265, 112671.
- Guanter, L., Kaufmann, H., Segl, K., Foerster, S., Rogass, C., Chabrillat, S., Kuester, T., Hollstein, A., Rossner, G., Chlebek, C., et al., 2015. The enmap spaceborne imaging spectroscopy mission for earth observation. *Remote Sensing* 7, 8830–8857.
- Guo, Y., Cao, X., Liu, B., Gao, M., 2020. Cloud detection for satellite imagery using attention-based u-net convolutional neural network. *Symmetry* 12, 1056.
- He, K., Gkioxari, G., Dollár, P., Girshick, R., 2017. Mask r-cnn, in: *Proceedings of the IEEE international conference on computer vision*, pp. 2961–2969.
- He, K., Zhang, X., Ren, S., Sun, J., 2016. Deep residual learning for image recognition, in: *Proceedings of the IEEE conference on computer vision and pattern recognition*, pp. 770–778.
- Hodson, T.O., 2022. Root mean square error (rmse) or mean absolute error (mae): When to use them or not. *Geoscientific Model Development Discussions* 2022, 1–10.
- Huang, B., Zhao, B., Song, Y., 2018. Urban land-use mapping using a deep convolutional neural network with high spatial resolution multispectral remote sensing imagery. *Remote Sensing of Environment* 214, 73–86.
- IEA, 2022. Global methane tracker 2022, iea, licence: Cc by 4.0. <https://www.iea.org/reports/global-methane-tracker-2022>. Accessed: 2024-05-15.
- IEA, 2024. Global methane tracker 2024, iea, paris, licence: Cc by 4.0. <https://www.iea.org/reports/global-methane-tracker-2024>. Accessed: 2024-05-15.
- Ihlen, V., 2019. Landsat 8 Data Users Handbook, LSDS-1574 Version 5.0. U.S. Geological Survey (USGS).
- Imasu, R., Matsunaga, T., Nakajima, M., Yoshida, Y., Shiomi, K., Morino, I., Saitoh, N., Niwa, Y., Someya, Y., Oishi, Y., et al., 2023. Greenhouse gases observing satellite 2 (gosat-2): mission overview. *Progress in Earth and Planetary Science* 10, 33.

- IMEO, 2022. Eye on methane 2022: International methane emissions observatory 2022.
- Irakulis-Loitxate, I., Guanter, L., Liu, Y.N., Varon, D.J., Maasackers, J.D., Zhang, Y., Chulakadabba, A., Wofsy, S.C., Thorpe, A.K., Duren, R.M., et al., 2021. Satellite-based survey of extreme methane emissions in the permian basin. *Science Advances* 7, eabf4507.
- Irakulis-Loitxate, I., Guanter, L., Maasackers, J.D., Zavala-Araiza, D., Aben, I., 2022. Satellites detect abatable super-emissions in one of the world’s largest methane hotspot regions. *Environmental Science & Technology* 56, 2143–2152.
- Irizar, J., Melf, M., Bartsch, P., Koehler, J., Weiss, S., Greinacher, R., Erdmann, M., Kirschner, V., Albinana, A.P., Martin, D., 2019. Sentinel-5/uvns, in: *International Conference on Space Optics—ICSO 2018*, SPIE. pp. 41–58.
- Jacob, D.J., Turner, A.J., Maasackers, J.D., Sheng, J., Sun, K., Liu, X., Chance, K., Aben, I., McKeever, J., Frankenberg, C., 2016. Satellite observations of atmospheric methane and their value for quantifying methane emissions. *Atmospheric Chemistry and Physics* 16, 14371–14396.
- Jacob, D.J., Varon, D.J., Cusworth, D.H., Dennison, P.E., Frankenberg, C., Gautam, R., Guanter, L., Kelley, J., McKeever, J., Ott, L.E., et al., 2022. Quantifying methane emissions from the global scale down to point sources using satellite observations of atmospheric methane. *Atmospheric Chemistry and Physics* 22, 9617–9646.
- Jervis, D., McKeever, J., Durak, B.O., Sloan, J.J., Gains, D., Varon, D.J., Ramier, A., Strupler, M., Tarrant, E., 2021. The ghgsat-d imaging spectrometer. *Atmospheric Measurement Techniques* 14, 2127–2140.
- de Jong, T.A., Maasackers, J.D., Irakulis-Loitxate, I., Randles, C.A., Tol, P., Aben, I., 2024. Daily global methane super-emitter detection and source identification with sub-daily tracking .
- Jongaramrungruang, S., Matheou, G., Thorpe, A.K., Zeng, Z.C., Frankenberg, C., 2021. Remote sensing of methane plumes: instrument tradeoff analysis for detecting and quantifying local sources at global scale. *Atmospheric Measurement Techniques* 14, 7999–8017.
- Jongaramrungruang, S., Thorpe, A.K., Matheou, G., Frankenberg, C., 2022. Methanet—an ai-driven approach to quantifying methane point-source emission from high-resolution 2-d plume imagery. *Remote Sensing of Environment* 269, 112809.

- Joyce, P., Ruiz Villena, C., Huang, Y., Webb, A., Gloor, M., Wagner, F.H., Chipperfield, M.P., Barrio Guilló, R., Wilson, C., Boesch, H., 2023. Using a deep neural network to detect methane point sources and quantify emissions from prisma hyperspectral satellite images. *Atmospheric Measurement Techniques* 16, 2627–2640.
- Junayed, M.S., Sadeghzadeh, A., Islam, M.B., Wong, L.K., Aydın, T., 2022. Himode: A hybrid monocular omnidirectional depth estimation model, in: *Proceedings of the IEEE/CVF Conference on Computer Vision and Pattern Recognition*, pp. 5212–5221.
- Krings, T., Gerilowski, K., Buchwitz, M., Hartmann, J., Sachs, T., Erzinger, J., Burrows, J., Bovensmann, H., 2013. Quantification of methane emission rates from coal mine ventilation shafts using airborne remote sensing data. *Atmospheric Measurement Techniques* 6, 151–166.
- Krings, T., Gerilowski, K., Buchwitz, M., Reuter, M., Tretner, A., Erzinger, J., Heinze, D., Pflüger, U., Burrows, J., Bovensmann, H., 2011. Mamap—a new spectrometer system for column-averaged methane and carbon dioxide observations from aircraft: retrieval algorithm and first inversions for point source emission rates. *Atmospheric Measurement Techniques* 4, 1735–1758.
- Kumar, S., Arevalo, I., Iftekhhar, A., Manjunath, B., 2023. Methanemapper: Spectral absorption aware hyperspectral transformer for methane detection, in: *Proceedings of the IEEE/CVF Conference on Computer Vision and Pattern Recognition*, pp. 17609–17618.
- Kumar, S., Torres, C., Ulutan, O., Ayasse, A., Roberts, D., Manjunath, B., 2020. Deep remote sensing methods for methane detection in overhead hyperspectral imagery, in: *Proceedings of the IEEE/CVF Winter Conference on Applications of Computer Vision*, pp. 1776–1785.
- Lauvaux, T., Giron, C., Mazzolini, M., d’Aspremont, A., Duren, R., Cusworth, D., Shindell, D., Ciais, P., 2022. Global assessment of oil and gas methane ultra-emitters. *Science* 375, 557–561.
- Li, A., Yang, J., Li, X., 2023. Cloud detection from remote sensing images by cascaded u-shape attention networks, in: *International Conference on Image and Graphics*, Springer. pp. 155–166.
- Li, J., Roy, D.P., 2017. A global analysis of sentinel-2a, sentinel-2b and landsat-8 data revisit intervals and implications for terrestrial monitoring. *Remote Sensing* 9, 902.
- Li, L., Chen, Y., Fan, L., Sun, D., He, H., Dai, Y., Wan, Y., Chen, F., 2024. A high-precision retrieval method for methane vertical profiles based on dual-band spectral data from the gosat satellite. *Atmospheric Environment* 317, 120183.

- Li, L., Li, X., Jiang, L., Su, X., Chen, F., 2021. A review on deep learning techniques for cloud detection methodologies and challenges. *Signal, Image and Video Processing* 15, 1527–1535.
- Lin, T.Y., Maire, M., Belongie, S., Hays, J., Perona, P., Ramanan, D., Dollár, P., Zitnick, C.L., 2014. Microsoft coco: Common objects in context, in: *Computer Vision–ECCV 2014: 13th European Conference, Zurich, Switzerland, September 6–12, 2014, Proceedings, Part V* 13, Springer. pp. 740–755.
- Liu, Y.N., Sun, D.X., Hu, X.N., Ye, X., Li, Y.D., Liu, S.F., Cao, K.Q., Chai, M.Y., Zhang, J., Zhang, Y., et al., 2019. The advanced hyperspectral imager: aboard china’s gaofen-5 satellite. *IEEE Geoscience and Remote Sensing Magazine* 7, 23–32.
- Liu, Z., Lin, Y., Cao, Y., Hu, H., Wei, Y., Zhang, Z., Lin, S., Guo, B., 2021. Swin transformer: Hierarchical vision transformer using shifted windows, in: *Proceedings of the IEEE/CVF international conference on computer vision*, pp. 10012–10022.
- Lorente, A., Borsdorff, T., Butz, A., Hasekamp, O., Aan De Brugh, J., Schneider, A., Wu, L., Hase, F., Kivi, R., Wunch, D., et al., 2021. Methane retrieved from tropomi: improvement of the data product and validation of the first 2 years of measurements. *Atmospheric Measurement Techniques* 14, 665–684.
- Mahajan, S., Fataniya, B., 2020. Cloud detection methodologies: Variants and development—a review. *Complex & Intelligent Systems* 6, 251–261.
- Monforti Ferrario, F., Crippa, M., Guizzardi, D., Muntean, M., Schaaf, E., Lo Vullo, E., Solazzo, E., Olivier, J., Vignati, E., 2021. Monforti ferrario, fabio; crippa, monica; guizzardi, diego; muntean, marilena; schAAF, edwin; lo vullo, eleonora; solazzo, efisio; olivier, jos; vignati, elisabetta (2021): Edgar v6.0 greenhouse gas emissions. european commission, joint research centre (jrc) [dataset]. <http://data.europa.eu/89h/97a67d67-c62e-4826-b873-9d972c4f670b>. Accessed: 2024-05-15.
- NASA, 2022. Nasa press release about geocarb cancellation 2022. <https://www.nasa.gov/news-release/nasa-to-cancel-geocarb-mission-expands-greenhouse-gas-portfolio/>. Accessed: 2024-04-24.
- Naser, M., Alavi, A.H., 2023. Error metrics and performance fitness indicators for artificial intelligence and machine learning in engineering and sciences. *Architecture, Structures and Construction* 3, 499–517.
- NIES, N.I.f.E.S., 2024. GOSAT-GW website. <https://gosat-gw.nies.go.jp/en/gosat-gw02.html#Satellite>. Accessed: 2024-06-04.

- Pandey, S., van Nistelrooij, M., Maasackers, J.D., Sutar, P., Houweling, S., Varon, D.J., Tol, P., Gains, D., Worden, J., Aben, I., 2023. Daily detection and quantification of methane leaks using sentinel-3: a tiered satellite observation approach with sentinel-2 and sentinel-5p. *Remote Sensing of Environment* 296, 113716.
- Parker, R.J., Webb, A., Boesch, H., Somkuti, P., Barrio Guillo, R., Di Noia, A., Kalaitzi, N., Anand, J.S., Bergamaschi, P., Chevallier, F., et al., 2020. A decade of gosat proxy satellite ch 4 observations. *Earth System Science Data* 12, 3383–3412.
- Prather, M.J., Holmes, C.D., Hsu, J., 2012. Reactive greenhouse gas scenarios: Systematic exploration of uncertainties and the role of atmospheric chemistry. *Geophysical Research Letters* 39.
- Qiu, S., Zhu, Z., He, B., 2019. Fmask 4.0: Improved cloud and cloud shadow detection in landsats 4–8 and sentinel-2 imagery. *Remote Sensing of Environment* 231, 111205.
- Radman, A., Mahdianpari, M., Varon, D.J., Mohammadimanesh, F., 2023. S2metnet: A novel dataset and deep learning benchmark for methane point source quantification using sentinel-2 satellite imagery. *Remote Sensing of Environment* 295, 113708.
- Rainio, O., Teuvo, J., Klén, R., 2024. Evaluation metrics and statistical tests for machine learning. *Scientific Reports* 14, 6086.
- Roger, J., Guanter, L., Gorroño, J., Irakulis-Loitxate, I., 2023a. Exploiting the entire near-infrared spectral range to improve the detection of methane plumes with high-resolution imaging spectrometers. *Atmospheric Measurement Techniques Discussions* 2023, 1–21.
- Roger, J., Irakulis-Loitxate, I., Valverde, A., Gorroño, J., Chabrillat, S., Brell, M., Guanter, L., 2023b. High-resolution methane mapping with the enmap satellite imaging spectroscopy mission .
- Roger, J., Irakulis-Loitxate, I., Valverde, A., Gorroño, J., Chabrillat, S., Brell, M., Guanter, L., 2024. High-resolution methane mapping with the enmap satellite imaging spectroscopy mission. *IEEE Transactions on Geoscience and Remote Sensing* .
- Ronneberger, O., Fischer, P., Brox, T., 2015. U-net: Convolutional networks for biomedical image segmentation, in: *Medical image computing and computer-assisted intervention—MICCAI 2015: 18th international conference, Munich, Germany, October 5-9, 2015, proceedings, part III* 18, Springer. pp. 234–241.
- Rouet-Leduc, B., Hulbert, C., 2024. Automatic detection of methane emissions in multispectral satellite imagery using a vision transformer. *Nature Communications* 15, 1–9.

- Rouet-Leduc, B., Kerdreux, T., Tuel, A., Hulbert, C., 2023. Autonomous detection of methane emissions in multispectral satellite data using deep learning. arXiv preprint arXiv:2308.11003 .
- Růžička, V., Mateo-Garcia, G., Gómez-Chova, L., Vaughan, A., Guanter, L., Markham, A., 2023. Semantic segmentation of methane plumes with hyperspectral machine learning models. *Scientific Reports* 13, 19999.
- Sánchez-García, E., Gorroño, J., Irakulis-Loitxate, I., Varon, D.J., Guanter, L., 2022. Mapping methane plumes at very high spatial resolution with the worldview-3 satellite. *Atmospheric Measurement Techniques* 15, 1657–1674.
- Sandler, M., Howard, A., Zhu, M., Zhmoginov, A., Chen, L.C., 2018. Mobilenetv2: Inverted residuals and linear bottlenecks, in: *Proceedings of the IEEE conference on computer vision and pattern recognition*, pp. 4510–4520.
- Sayler, K., 2022. *Landsat 9 Data Users Handbook, LSDS-2082 Version 1.0*. U.S. Geological Survey (USGS).
- Scarpelli, T.R., Jacob, D.J., Grossman, S., Lu, X., Qu, Z., Sulprizio, M.P., Zhang, Y., Reuland, F., Gordon, D., Worden, J.R., 2022. Updated global fuel exploitation inventory (gfei) for methane emissions from the oil, gas, and coal sectors: evaluation with inversions of atmospheric methane observations. *Atmospheric Chemistry and Physics* 22, 3235–3249.
- Schmit, T.J., Griffith, P., Gunshor, M.M., Daniels, J.M., Goodman, S.J., Lebar, W.J., 2017. A closer look at the abi on the goes-r series. *Bulletin of the American Meteorological Society* 98, 681–698.
- Schmit, T.J., Lindstrom, S.S., Gerth, J.J., Gunshor, M.M., 2018. Applications of the 16 spectral bands on the advanced baseline imager (abi) .
- Schuit, B.J., Maasakkers, J.D., Bijl, P., Mahapatra, G., Van den Berg, A.W., Pandey, S., Lorente, A., Borsdorff, T., Houweling, S., Varon, D.J., et al., 2023. Automated detection and monitoring of methane super-emitters using satellite data. *Atmospheric Chemistry and Physics Discussions* , 1–47.
- Sherwin, E.D., El Abbadi, S.H., Burdeau, P.M., Zhang, Z., Chen, Z., Rutherford, J.S., Chen, Y., Brandt, A.R., 2024. Single-blind test of nine methane-sensing satellite systems from three continents. *Atmospheric Measurement Techniques* 17, 765–782.
- Shindell, D., Kuylenstierna, J.C., Vignati, E., van Dingenen, R., Amann, M., Klimont, Z., Anenberg, S.C., Muller, N., Janssens-Maenhout, G., Raes, F., et al., 2012. Simultaneously mitigating near-term climate change and improving human health and food security. *Science* 335, 183–189.

- Si, G., Fu, S., Yao, W., 2024. Unlocking the potential: Multi-task deep learning for spaceborne quantitative monitoring of fugitive methane plumes. arXiv preprint arXiv:2401.12870 .
- Sierk, B., Fernandez, V., Bézy, J.L., Meijer, Y., Durand, Y., Courrèges-Lacoste, G.B., Pachot, C., Löscher, A., Nett, H., Minoglou, K., et al., 2021. The copernicus co2m mission for monitoring anthropogenic carbon dioxide emissions from space, in: International Conference on Space Optics—ICSO 2020, SPIE. pp. 1563–1580.
- Simonyan, K., Zisserman, A., 2014. Very deep convolutional networks for large-scale image recognition. arXiv preprint arXiv:1409.1556 .
- Song, Q., Ma, C., Liu, J., Wei, H., 2022. Quantifying ocean surface green tides using high-spatial resolution thermal images. *Optics Express* 30, 36592–36602.
- Staebell, C., Sun, K., Samra, J., Franklin, J., Chan Miller, C., Liu, X., Conway, E., Chance, K., Milligan, S., Wofsy, S., 2021. Spectral calibration of the methaneair instrument. *Atmospheric Measurement Techniques* 14, 3737–3753.
- Staniaszek, Z., Griffiths, P.T., Folberth, G.A., O’Connor, F.M., Abraham, N.L., Archibald, A.T., 2022. The role of future anthropogenic methane emissions in air quality and climate. *Npj Climate and Atmospheric Science* 5, 21.
- Szegedy, C., Liu, W., Jia, Y., Sermanet, P., Reed, S., Anguelov, D., Erhan, D., Vanhoucke, V., Rabinovich, A., 2015. Going deeper with convolutions, in: Proceedings of the IEEE conference on computer vision and pattern recognition, pp. 1–9.
- Tan, J., NourEldeen, N., Mao, K., Shi, J., Li, Z., Xu, T., Yuan, Z., 2019. Deep learning convolutional neural network for the retrieval of land surface temperature from amsr2 data in china. *Sensors* 19, 2987.
- Tan, M., Le, Q., 2021. Efficientnetv2: Smaller models and faster training, in: International conference on machine learning, PMLR. pp. 10096–10106.
- Thompson, D., Thorpe, A., Frankenberg, C., Green, R., Duren, R., Guanter, L., Hollstein, A., Middleton, E., Ong, L., Ungar, S., 2016. Space-based remote imaging spectroscopy of the aliso canyon ch4 superemitter. *Geophysical Research Letters* 43, 6571–6578.
- Thompson, D.R., Green, R.O., Bradley, C., Brodrick, P.G., Mahowald, N., Dor, E.B., Bennett, M., Bernas, M., Carmon, N., Chadwick, K.D., Clark, R.N., Coleman, R.W., Cox, E., Diaz, E., Eastwood, M.L., Eckert, R., Ehlmann, B.L., Ginoux, P., Ageitos, M.G., Grant, K., et al., 2024. On-orbit calibration and performance of the emit imaging spectrometer. *Remote Sensing of Environment* 303, 113986. doi:<https://doi.org/10.1016/j.rse.2023.113986>.

- Thompson, D.R., Karpatne, A., Ebert-Uphoff, I., Frankenberg, C., Thorpe, A.K., Bue, B.D., Green, R.O., 2017. Is-geo dataset jpl-ch4-detection-2017-v1. 0: A benchmark for methane source detection from imaging spectrometer data .
- Thorpe, A., Frankenberg, C., Roberts, D., 2014. Retrieval techniques for airborne imaging of methane concentrations using high spatial and moderate spectral resolution: Application to aviris. *Atmospheric Measurement Techniques* 7, 491–506.
- Thorpe, A.K., Duren, R.M., Conley, S., Prasad, K.R., Bue, B.D., Yadav, V., Foster, K.T., Rafiq, T., Hopkins, F.M., Smith, M.L., et al., 2020. Methane emissions from underground gas storage in california. *Environmental Research Letters* 15, 045005.
- Thorpe, A.K., Frankenberg, C., Aubrey, A., Roberts, D., Nottrott, A., Rahn, T., Sauer, J., Dubey, M., Costigan, K., Arata, C., et al., 2016. Mapping methane concentrations from a controlled release experiment using the next generation airborne visible/infrared imaging spectrometer (aviris-ng). *Remote Sensing of Environment* 179, 104–115.
- Thorpe, A.K., Green, R.O., Thompson, D.R., Brodrick, P.G., Chapman, J.W., Elder, C.D., Irakulis-Loitxate, I., Cusworth, D.H., Ayasse, A.K., Duren, R.M., et al., 2023. Attribution of individual methane and carbon dioxide emission sources using emit observations from space. *Science Advances* 9, eadh2391.
- Tratt, D.M., Buckland, K.N., Hall, J.L., Johnson, P.D., Keim, E.R., Leifer, I., Westberg, K., Young, S.J., 2014. Airborne visualization and quantification of discrete methane sources in the environment. *Remote sensing of environment* 154, 74–88.
- Ubierna, M., Montesino, M., Ocerin, E., Fabrizi, R., Fernandez, T.M., 2022. Gei-sat constellation for greenhouse gases detection and quantification .
- Vanselow, S., Schneising, O., Buchwitz, M., Reuter, M., Bovensmann, H., Boesch, H., Burrows, J.P., 2024. Automated detection of regions with persistently enhanced methane concentrations using sentinel-5 precursor satellite data. *Atmospheric Chemistry & Physics Discussions* .
- Varon, D., McKeever, J., Jervis, D., Maasackers, J., Pandey, S., Houweling, S., Aben, I., Scarpelli, T., Jacob, D., 2019. Satellite discovery of anomalously large methane point sources from oil/gas production. *Geophysical Research Letters* 46, 13507–13516.
- Varon, D.J., Jacob, D.J., McKeever, J., Jervis, D., Durak, B.O., Xia, Y., Huang, Y., 2018. Quantifying methane point sources from fine-scale satellite observations of atmospheric methane plumes. *Atmospheric Measurement Techniques* 11, 5673–5686.

- Varon, D.J., Jervis, D., McKeever, J., Spence, I., Gains, D., Jacob, D.J., 2021. High-frequency monitoring of anomalous methane point sources with multispectral sentinel-2 satellite observations. *Atmospheric Measurement Techniques* 14, 2771–2785.
- Vaswani, A., Shazeer, N., Parmar, N., Uszkoreit, J., Jones, L., Gomez, A.N., Kaiser, L., Polosukhin, I., 2017. Attention is all you need. *Advances in neural information processing systems* 30.
- Vaughan, A., Mateo-García, G., Gómez-Chova, L., Ružička, V., Guanter, L., Irakulis-Loitxate, I., 2024. Ch4net: a deep learning model for monitoring methane super-emitters with sentinel-2 imagery. *Atmospheric Measurement Techniques* 17, 2583–2593. URL: <https://amt.copernicus.org/articles/17/2583/2024/>, doi:10.5194/amt-17-2583-2024.
- Wang, H., Fan, X., Jian, H., Yan, F., 2024. Exploiting the matched filter to improve the detection of methane plumes with sentinel-2 data. *Remote Sensing* 16, 1023.
- Watine-Guiu, M., Varon, D.J., Irakulis-Loitxate, I., Balasus, N., Jacob, D.J., 2023. Geostationary satellite observations of extreme and transient methane emissions from oil and gas infrastructure. *Proceedings of the National Academy of Sciences* 120, e2310797120.
- WMO, 2024. WMO gho constellation imager. https://space.oscar.wmo.int/instruments/view/ghost_imager. Accessed: 2024-03-12.
- Worden, J., Turner, A., Bloom, A., Kulawik, S., Liu, J., Lee, M., Weidner, R., Bowman, K., Frankenberg, C., Parker, R., et al., 2015. Quantifying lower tropospheric methane concentrations using gosat near-ir and tes thermal ir measurements. *Atmospheric Measurement Techniques* 8, 3433–3445.
- Worden, J., Wecht, K., Frankenberg, C., Alvarado, M., Bowman, K., Kort, E., Kulawik, S., Lee, M., Payne, V., Worden, H., 2013. Ch 4 and co distributions over tropical fires during october 2006 as observed by the aura tes satellite instrument and modeled by geos-chem. *Atmospheric Chemistry and Physics* 13, 3679–3692.
- Xie, F., Shi, M., Shi, Z., Yin, J., Zhao, D., 2017. Multilevel cloud detection in remote sensing images based on deep learning. *IEEE Journal of Selected Topics in Applied Earth Observations and Remote Sensing* 10, 3631–3640.
- Yang, Y., Shang, K., Xiao, C., Wang, C., Tang, H., 2022. Spectral index for mapping topsoil organic matter content based on zy1-02d satellite hyperspectral data in jiangsu province, china. *ISPRS International Journal of Geo-Information* 11, 111.

- Ye, H., Shi, H., Wang, X., Sun, E., Li, C., An, Y., Wu, S., Xiong, W., Li, Z., Landgraf, J., 2023. Improving atmospheric co2 retrieval based on the collaborative use of greenhouse gases monitoring instrument and directional polarimetric camera sensors on chinese hyperspectral satellite gf5-02. *Geo-Spatial Information Science*, 1–13.
- Yu, J., Hmiel, B., Lyon, D.R., Warren, J., Cusworth, D.H., Duren, R.M., Chen, Y., Murphy, E.C., Brandt, A.R., 2022. Methane emissions from natural gas gathering pipelines in the permian basin. *Environmental Science & Technology Letters* 9, 969–974.
- Zavala-Araiza, D., Lyon, D., Alvarez, R.A., Palacios, V., Harriss, R., Lan, X., Talbot, R., Hamburg, S.P., 2015. Toward a functional definition of methane super-emitters: Application to natural gas production sites. *Environmental science & technology* 49, 8167–8174.
- Zhang, Z., Cusworth, D.H., Ayasse, A.K., Sherwin, E.D., Brandt, A.R., 2023. Measuring carbon dioxide emissions from liquefied natural gas (lng) terminals with imaging spectroscopy. *Geophysical Research Letters* 50, e2023GL105755.
- Zhang, Z., Sherwin, E.D., Varon, D.J., Brandt, A.R., 2022. Detecting and quantifying methane emissions from oil and gas production: algorithm development with ground-truth calibration based on sentinel-2 satellite imagery. *Atmospheric Measurement Techniques* 15, 7155–7169.
- Zhou, B., Khosla, A., Lapedriza, A., Oliva, A., Torralba, A., 2016. Learning deep features for discriminative localization, in: *Proceedings of the IEEE conference on computer vision and pattern recognition*, pp. 2921–2929.
- Zhu, X.X., Xiong, Z., Wang, Y., Stewart, A.J., Heidler, K., Wang, Y., Yuan, Z., Dujardin, T., Xu, Q., Shi, Y., 2024. On the foundations of earth and climate foundation models. *arXiv preprint arXiv:2405.04285*.
- Zhuang, C., Lu, Z., Wang, Y., Xiao, J., Wang, Y., 2022. Acdnet: Adaptively combined dilated convolution for monocular panorama depth estimation, in: *Proceedings of the AAAI Conference on Artificial Intelligence*, pp. 3653–3661.

Appendix A. List of Acronyms

List of Acronyms

- ABI** Advanced Baseline Imager. 8, 12
- AHSI** Advanced Hyperspectral Imager. 5, 8
- AP** Average Precision. 22
- ARE** Absolute Relative Error. 30
- ASI** Italian Space Agency. 6, 8
- AUPRC** Area under the Precision-Recall Curve. 22
- AVIRIS** Airborne Visible Infrared Imaging Spectrometer. 9, 10, 13, 14, 16
- AVIRIS-NG** Airborne Visible Infrared Imaging Spectrometer - Next Generation.
5, 9, 10, 13, 21, 22, 24–29, 35
- CAST** China Academy of Space Technology. 6
- CH₄** Chemical formula for Methane. 1, 2, 17, 27
- CHIME** Copernicus Hyperspectral Imaging Mission. 11
- CNN** Convolutional Neural Networks. 4, 20, 21, 23, 24, 26, 27, 30–32, 35
- CNSA** China National Space Agency. 6, 8
- CO₂M** Copernicus Anthropogenic Carbon Dioxide Monitoring constellation. 11
- CO₂** Chemical formula for Carbon Dioxide. 1, 2, 11, 14, 15, 21, 34
- COCO** Common Objects in Context. 26
- CRESDA** China Center for Resources Satellite Data and Application. 6, 8
- DETR** Detection transformer. 26
- DLR** German Aerospace Center. 6, 8
- ECMWF** European Centre for Medium-Range Weather Forecasts. 30
- EDF** European Defence Fund. 6, 8
- EMIT** Earth Surface Mineral Dust Source Investigation. 5, 8, 10, 13

EnMAP Environmental Mapping and Analysis Program. 5, 8, 13, 21, 22, 26, 28

EOL End of Life. 6

ESA European Space Agency. 6, 8

FNR False Negative Rate. 22

FPR False Positive Rate. 22

FWHM Full Width at Half Maximum. 7, 11

GAO Global Airborne Observatory. 26

GeiSAT P GeiSAT Precursor. 9, 10, 13

GFS Global Forecast System. 30

GHOS_t Global Hyperspectral Observation Satellite. 9, 10

GMI Greenhouse-gases Monitoring Instrument. 5, 8

GOES Geostationary Operational Environmental Satellites. 5, 6, 8, 10, 12

GOSAT Greenhouse Gases Observing Satellite. 5, 6, 8, 10, 12, 13, 15

GOSAT-GW Global Observing Satellite for Greenhouse gases and Water cycle. 11, 12

GSD Ground Sampling Distance. 5, 6, 10–13

HI Hyperspectral imager. 9

HSI Hyperspectral Imager. 8

HYC HYperspectral Camera. 8

IME Integrated Mass Enhancement. 3, 4, 18, 19, 28, 31–33, 35

IoU Intersection over Union. 22

ISS International Space Station. 5, 10, 11

JAXA Japan Aerospace Exploration Agency. 6, 8

JPL Jet Propulsion Laboratory. 6, 9

MAE Mean Absolute Error. 29

mAP median Average Precision. 22

MAPE Mean Absolute Percentage Error. 29

MBMP Multi-Band-Multi-Pass. 16, 25, 26

MBSP Multi-Band-Single-Pass. 15, 16

MERLIN Methane Remote Sensing Lidar Mission. 11

mIoU mean Intersection over Union. 22

ML Machine Learning. 3, 4, 7, 20, 21, 23, 24, 27–30, 32–35

MLP Multi-Layer Perceptrons. 20, 21, 23, 24, 26, 27, 30, 31

MLR Multiple Linear Regression. 30

MODTRAN Moderate resolution atmospheric Transmission. 17

MSI Multispectral Instrument. 8

NASA National Aeronautics and Space Administration. 6, 8, 9, 11

NO_x Nitrogen oxides. 24, 34

NOAA National Oceanic and Atmospheric Administration. 6, 8, 10, 13

NWS American National Weather Service. 30

NZSA New Zealand Space Agency. 6, 8

OLI Operational Land Imager. 8, 10

POSP Particulate Observing Scanning Polarimeter. 8

PRISMA Pecursore Iperspettrale della Missione Applicativa. 5, 8, 13, 24–26, 28

R Pearson correlation coefficient. 29

RGB Red-green-blue. 22, 26, 35

RMSE Root mean squared Error. 29, 30, 35

RS Remote Sensing. 23

SBMP Single-Band-Multiple-Pass. 15

Sentinel 5P Sentinel-5 Precursor. 5, 6, 8, 10, 12, 13, 20, 22, 24

SLSTR Sea and Land Surface Temperature Radiometer. 8

SNR Signal-to-Noise Ratio. 22, 25–27

SRON Netherlands Institute for Space Research. 20

SVM Support Vector Machines. 23, 24, 30

SWIR Short-Wave Infrared. 2, 3, 5, 14

Tango Twin Anthropogenic Greenhouse Gas Observers. 11, 13

TANSO-FTS Thermal And Near infrared Sensor for carbon Observations - Fourier Transform Spectrometer. 8

TIR Thermal Infrared. 2, 3

TPR True Positive Rate. 22

TROPOMI TROPOspheric Monitoring Instrument. 8

USGS United States Geological Survey. 6, 8

VGG-16 Visual Geometry Group 16. 23

VIIRS Visible Infrared Imaging Radiometer Suite. 8

WAF-P Wide-Angle Fabry-Perot. 8